

# CIC: Circular Image Compression

Honggui LI<sup>1\*</sup>, Sinan CHEN<sup>2</sup>, Nahid MD LOKMAN HOSSAIN<sup>3</sup>, Maria TROCAN<sup>4</sup>, Beata MIKOVICOVA<sup>5</sup>, Muhammad FAHIMULLAH<sup>6</sup>, Dimitri GALAYKO<sup>7</sup>, Mohamad SAWAN<sup>8,9</sup>

<sup>1,2,3</sup>School of Information Engineering, Yangzhou University, Yangzhou 225127, China

<sup>4,5,6</sup>LISITE Research Lab, Institut Supérieur d'Électronique de Paris, Paris 75006, France

<sup>7</sup>Laboratoire d'Informatique de Paris 6, Sorbonne University, Paris 75020, France

<sup>8</sup>Polystim Neurotech Laboratory, Polytechnique Montreal, Montreal H3T1J4, Canada

<sup>9</sup>School of Engineering, Westlake University, Hangzhou 310024, China

<sup>1</sup>hgli@yzu.edu.cn, <sup>2</sup>32234352677@qq.com, <sup>3</sup>mh23083@stu.yzu.edu.cn, <sup>4</sup>maria.trocan@isep.fr,

<sup>5</sup>beata.mikovicova@isep.fr, <sup>6</sup>muhammad.fahimullah@ext.isep.fr, <sup>7</sup>dimitri.galayko@sorbonne-

universite.fr, <sup>8</sup>mohamad.sawan@polymtl.ca, <sup>9</sup>sawan@westlake.edu.cn

\*Corresponding Author

**Abstract:** Learned image compression (LIC) is currently the cutting-edge method. However, the inherent difference between testing and training images of LIC results in performance degradation to some extent. Especially for out-of-sample, out-of-distribution, or out-of-domain testing images, the performance of LIC dramatically degraded. Classical LIC is a serial image compression (SIC) approach that utilizes an open-loop architecture with serial encoding and decoding units. Nevertheless, according to the theory of automatic control, a closed-loop architecture holds the potential to improve the dynamic and static performance of LIC. Therefore, a circular image compression (CIC) approach with closed-loop encoding and decoding elements is proposed to minimize the gap between testing and training images and upgrade the capability of LIC. The proposed CIC establishes a nonlinear loop equation and proves that steady-state error between reconstructed and original images is close to zero by Talor series expansion. The proposed CIC method possesses the property of Post-Training and plug-and-play which can be built on any existing advanced SIC methods. Experimental results on five public image compression datasets demonstrate that the proposed CIC outperforms five open-source state-of-the-art competing SIC algorithms in reconstruction capacity. Experimental results further show that the proposed method is suitable for out-of-sample testing images with dark backgrounds, sharp edges, high contrast, grid shapes, or complex patterns.

**Keywords:** Learned Image Compression, Circular Image Compression, Steady-State Error, Taylor Series Expansion, Plug-and-Play

## 1 Introduction

In the current world of big data and generative artificial intelligence, a large amount of images are produced in various ways moment by moment [1]. Hence, it is necessary to efficiently compress images before transmission, storage, analysis, processing, recognition, and understanding [2-3]. Image compression methods can be divided into two categories: lossy and lossless image

compression [4]. The former seeks for the balance between bitrate and distortion, the latter seeks for minimum bitrate without distortion. Image compression methods can also be partitioned into two categories: model-based image compression and learning-based image compression [5]. The former develops to the full, and the latter is the front research direction and can be named as end-to-end deep learning-based image compression, learning-driven image compression, or learned image compression (LIC).

Because LIC is data-driven, deep neural network is firstly optimized by training image datasets and finally evaluated by testing image datasets. Training and testing image datasets hold similar but not identical characteristics. Deep neural network is optimal for training image datasets and is not always optimal for testing image datasets. Thus, the discrepancy between testing and training image datasets leads to performance degradation to some degree. Particularly for out-of-sample, out-of-distribution, or out-of-domain testing images, the performance of LIC dramatically degrades [6-8]. Hence, it is vitally important to improve the output of trained deep neural network based on testing image datasets to achieve ideal image reconstruction performance.

LIC usually utilizes an open-loop architecture with serial encoding and decoding units and can be named as serial image compression (SIC). Closed-loop architecture is widely adopted in automatic control systems to obtain extraordinary static and dynamic performance. According to the theory of automatic control, closed-loop architecture is superior to open-loop architecture in steady and transient states capability [9-10]. Therefore, circular image compression (CIC) method with closed-loop encoding and decoding elements is proposed to minimize the gap between training and testing image datasets and improve the reconstruction performance of LIC.

The proposed CIC is described by a nonlinear loop equation which is resolved by Taylor series expansion. Taylor series is an efficient tool for nonlinear analysis and has already been used for deep learning and LIC [11-12]. Wei PX et al propose a Taylor neural network with Taylor series approximation [11]. Bao YE et al present a Taylor series expansion of sinusoidal functions based two-branch nonlinear transformation architecture to eliminate correlations from images [12].

In the present realm of large language models, there are many excellent pretrained SIC models which are openly and freely released on the Internet, such as GitHub and HuggingFace. It provides the opportunity to upgrade the performance of the pretrained SIC models in the way of plug-and-play and Post-Training. Actually, plug-and-play policy is widely employed in deep learning-based image restoration including the decoding of lossy image compression [13-18]. The proposed CIC can be built on any existing advanced pretrained SIC models and lift their performance in the form of plug-and-play and Post-Training.

The key innovations of this paper are listed as follows:

- (1) closed-loop CIC framework with encoding and decoding elements;
- (2) plug-and-play and Post-Training attribution established on any leading pretrained SIC models;
- (3) nonlinear loop equation and complete mathematical proof of zero steady-state error with linear approximation of Taylor series expansion;
- (4) huge performance boost in peak signal-to-noise ratio (PSNR), structural similarity (SSIM), and

bits per sub pixel (BPSP); absolute and logic difference image blocks which demonstrate the extraordinary reconstruction capability.

The remainder of this paper is arranged as follows. The related work is reviewed in section 2, the theoretical fundamentals are elaborated in section 3, the evaluation experiment is conducted in section 4, and the summary and prospect are discussed in section 5.

## 2 Related Work

With the swift progress of deep learning theory and technology, LIC methods continuously improve their performance [19-43]. These methods can be divided into two categories: In-Training and Post-Training based methods. The former enhances LIC performance during training procedure, the latter enhances LIC performance after training procedure or during testing procedure. Both In-Training and Post-Training methods focus on encoding-decoding network architectures, entropy models of latent representations, quantization policies, attention mechanisms, and etc.

In-Training based LIC methods utilize some state-of-the-art generative models, such as diffusion model, flow model, autoregressive model, generative adversarial network (GAN), variance autoencoder (VAE), residual network (ResNet) based model, transformer-based model, convolutional neural network (CNN) based model, and so on [19-16]. Bai YC et al propose a VAE and autoregressive model based deep lossy plus residual coding method for both lossless and near-lossless image compression [19]. Yang RH et al present a lossy image compression approach with conditional diffusion model [20]. Bai YC et al also raise an end-to-end image compression algorithm with transformer-based model [21]. Zhang ZB et al put forward a decoupled framework-based image compression method that lets autoregressive model hold the capability of decoding in parallel [22]. Zhang DY et al come up with a resolution field-based reciprocal pyramid network for scalable image compression [23]. Guerin ND Jr et al propose a VAE-based LIC method that dynamically adapts loss parameters to mitigate rate estimation issues and ensure precise target bitrate attainment [24]. Zhang WC et al present a semantically disentangled ultra-low bitrate LIC codec by synthesizing multiple neural computing techniques such as style GAN, inverse GAN mapping, and contrastive disentangled representation learning [25]. Fu HS et al raise a flexible discretized Gaussian-Laplacian-Logistic mixture model for the latent representations, which can adapt to different contents in different images and different regions of one image more accurately and efficiently [26].

Some In-Training based LIC methods concentrate on quantization strategies of latent representations [27-32]. Duan ZH et al put forward a lossy image compression approach with quantized hierarchical VAE [27]. Timur A comes up with a vector quantized VAE for image compression [28]. Cai SL et al propose a flow model based invertible continuous codec for high-fidelity variable-bitrate image compression to avoid the usage of a set of different models for compressing images at different rates [29]. Fu HS et al present an asymmetric LIC algorithm with multi-scale residual block, importance scaling, and post-quantization filtering [30]. Zhang G et al raise an enhanced quantified local implicit neural representation for image compression by enhancing the utilization of local relationships of implicit neural representation and narrow the

quantization gap between training and encoding [31]. Guo JY et al put forward a new LIC framework that aims to learn one single network to support variable bitrate coding under various computational complexity levels [32].

Some In-Training based LIC methods are concerned with attention mechanisms [33-35]. Jiang ZY et al come up with a novel image compression autoencoder based on the local-global joint attention mechanism [33]. Li B et al propose LIC approach via neighborhood-based attention optimization and context modeling with multi-scale guiding [34]. Tang ZS et al present an end-to-end image compression method integrating graph attention and asymmetric CNN [35].

Pots-Training based LIC methods strengthen the performance of pretrained LIC models [36-39]. Shi JQ et al adopt a plug-and-play rate-distortion optimized Post-Training quantization to process pretrained, off-the-shelf LIC models and minimize quantization-induced error of model parameters [36]. Duan ZH et al raise a quantization-aware ResNet VAE for lossy image compression with test-time quantization and quantization-aware training [37]. Li SH et al put forward a progressive LIC algorithm with dead-zone quantizers on the latent representation which is successfully incorporated into existing pre-trained fixed-rate models without re-training [38]. Son H et al come up with an enhanced standard compatible image compression framework to fuse learnable codecs, postprocessing networks, and compact representation networks [39].

Some Pots-Training based LIC methods directly enhance the quality of decoded images of LIC [40-43]. Li JF et al propose a recurrent convolution network for blind image compression artifact reduction in industrial IoT systems [40]. Ma L et al present a sensitivity decouple learning approach for image compression artifacts reduction which decouples the intrinsic image attributes into compression-insensitive features for high-level semantics and compression-sensitive features for low-level cues [41]. Hu JH et al raise a ResNet for image compression artifact reduction [42]. Chen HG et al put forward a deep CNN for JPEG image compression artifacts reduction [43].

Some In-Training and Post-Training based LIC methods attempt to resolve the problem of out-of-sample, out-of-distribution, or out-of-domain testing images [7-8]. Li SH et al come up with a Post-Training pruning method based on the admissible range and in-distribution region to automatically remove the out-of-distribution channels for LIC [7]. Tsubota K et al propose a content-adaptive optimization framework for universal LIC which adapts a pretrained compression model to each target image during testing for addressing the domain gap between pretraining and post-testing [8].

In summary, this paper presents a Post-Training based lossy LIC method, CIC, to minimize the discrimination between testing and training image datasets and promote the performance of image reconstruction.

## **3 Theory**

### **3.1 Terminology Glossary**

The terminology abbreviations and mathematical notations employed in this paper are gathered in Table 1.

**Table 1. Summary of abbreviations & notations.**

| <b>Abbreviation &amp; Notation</b>                          | <b>Meaning</b>  |
|---|---|
| EN / DE   | Encoding / Decoding                                       |
| SIC / CIC   | Serial Image Compression / Circular Image Compression     |
| FB / NF   | FeedBack / Nonlinear Function                             |
| D / d   | Original Image Dimension / Encoded Image Dimension        |
| W / H / C   | Image Width / Image Height / Image Channels               |
| $\mathbf{f} / \mathbf{f}_e / \mathbf{f}_d$                  | Original Image / Encoded Image / Decoded Image            |
| $\mathbf{f}_r / \mathbf{f}_c$                               | Residual Term / Control Term                              |
| $\mathbf{f}_a / \mathbf{f}_l / \mathbf{f}_t / \mathbf{f}_r$ | Absolute / Logical / Testing / Reference difference Image |
| $\mathbf{o} / \mathbf{O}$                                   | First-Order Term / Higher-Order Term                      |
| $\mathbf{\Lambda} / \mathbf{U}$                             | Coefficient Matrix  |
| $t / \mathbf{r}$  | Time / Reconstruction Error                               |
| $N / \eta$  | Iteration Number / Iteration Constant                     |
| LIC   | Learned Image Compression                                 |
| VAE   | Variational Auto-Encoder                                  |
| DLPR  | Deep Lossy Plus Residual Coding                           |
| CDC   | Conditional Diffusion Compression                         |
| ICT   | Image Compression with Transformers                       |
| QRVAE   | Quantized ResNet Variational Auto-Encoders                |
| VQVAE   | Vector Quantized Variational Auto-Encoders                |
| PSNR  | Peak Signal-to-Noise Ratio                                |
| SSIM  | Structural Similarity                                     |
| BPSP  | Bits Per Sub Pixel  |

### 3.2 Theoretical Architecture

The proposed theoretical architecture of CIC is illustrated in Figure 1. It is a combination of open-loop and closed-loop architectures. It consists of two halves: the left half and the right half. The left half is the classical open-loop SIC framework and can also be named as linked or cascade image compression. The right half is the closed-loop CIC framework and can also be named as ringed or cycle image compression. SIC contains two units: encoding (EN) and decoding (DE). The EN unit compresses the original image to the encoded image and is composed of representation (RP), quantization (QT), and entropy coding (EC). The DE unit decompresses the encoded image to the decoded image and is composed of entropy decoding (ED) and reconstruction (RC). CIC incorporates five elements: EN, DE, summator, multiplier, and integrator. The EN and DE elements of CIC are the same as those of SIC. The summator introduces negative feedback into CIC. The multiplier, integrator, and summator implement the traditional proportion-integration-differentiation control. The input of the proposed architecture is original image  $\mathbf{f}_0$  and the output is reconstructed image  $\mathbf{f}$ . The proposed CIC can achieve better reconstruction images than those of the traditional SIC.

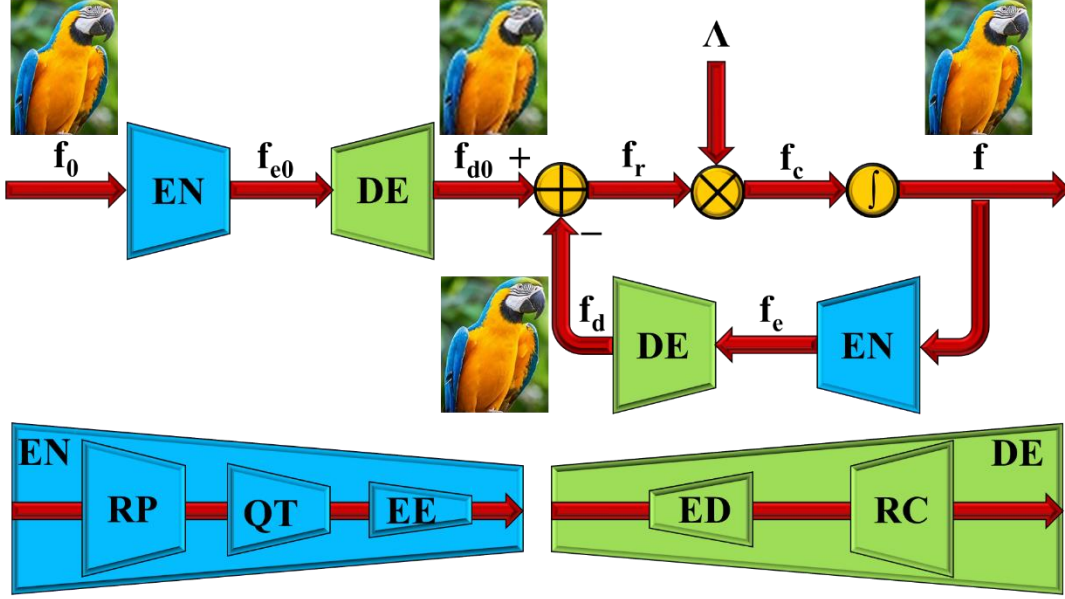


Figure 1. The theoretical architecture of CIC.

The CIC holds the property of plug-and-play and can be built on any existing advanced LIC methods. That is to say, CIC can take advantage of the EN and DE units of any pretrained LIC models. The SIC can be described by the following mathematical equations:

$$\begin{aligned}
 \mathbf{f}_{e0} &= \text{EN}(\mathbf{f}_0) \\
 \mathbf{f}_{d0} &= \text{DE}(\mathbf{f}_{e0}) \quad , \\
 \mathbf{f}_0, \mathbf{f}_{d0} &\in \mathbb{R}^D; \mathbf{f}_{e0} \in \mathbb{R}^d
 \end{aligned} \tag{1}$$

where:

EN is the encoder and is given in the classical SIC;

DE is the decoder and is also given in the classical SIC;

$\mathbf{f}_0$  is the original image;

$\mathbf{f}_{e0}$  is the encoded image after EN and is the true input of the proposed architecture;

$\mathbf{f}_{d0}$  is the decoded image after DE;

D is the dimension of  $\mathbf{f}_0$  and  $\mathbf{f}_{d0}$ ;

d is the dimension of  $\mathbf{f}_{e0}$ .

According to Equation (1), the nonlinear function (NF) of SIC from the input to the output can be depicted by the following mathematical expressions:

$$\begin{aligned}
 \mathbf{f}_{d0} &= \text{DE}(\text{EN}(\mathbf{f}_0)) = \text{NF}(\mathbf{f}_0) \\
 \text{NF}(\cdot) &= \text{DE}(\text{EN}(\cdot)) \quad . \\
 \text{NF}(\cdot) &\in \mathbb{R}^D
 \end{aligned} \tag{2}$$

The CIC can be portrayed by the following mathematical formulas:

$$\begin{aligned}
\mathbf{f}_e(t) &= \text{EN}(\mathbf{f}(t)) \\
\mathbf{f}_d(t) &= \text{DE}(\mathbf{f}_e(t)) \\
\mathbf{f}_r(t) &= \mathbf{f}_{d0} - \mathbf{f}_d(t) \\
\mathbf{f}_c(t) &= \mathbf{\Lambda}(t)\mathbf{f}_r(t)
\end{aligned} \tag{3}$$

$$\mathbf{f}(t) = \mathbf{f}(0) + \int_0^t \mathbf{f}_c(t) dt$$

$$\mathbf{\Lambda}(t) = \text{diag}(\mathbf{\Lambda}_{11}(t) \quad \mathbf{\Lambda}_{22}(t) \quad \cdots \quad \mathbf{\Lambda}_{DD}(t))$$

$$t \in \mathbf{R}; \mathbf{f}(t), \mathbf{f}_d(t), \mathbf{f}_r(t), \mathbf{f}_c(t) \in \mathbf{R}^D; \mathbf{f}_{d0} \in \mathbf{R}^D; \mathbf{\Lambda}(t) \in \mathbf{R}^{D \times D}$$

where:

$t$  represents the time;

$\mathbf{f}(t)$  represents the expected reconstructed image at time  $t$  and is the output of the proposed architecture;

$\mathbf{f}_e(t)$  represents the encoded image of  $\mathbf{f}(t)$  at time  $t$ ;

$\mathbf{f}_d(t)$  represents the decoded image of  $\mathbf{f}_e(t)$  at time  $t$ ;

$\mathbf{f}_r(t)$  represents the residual term at time  $t$ ;

$\mathbf{f}_c(t)$  represents the control term at time  $t$ ;

$\mathbf{f}(0)$  represents the initial value of  $\mathbf{f}(t)$  at time 0 and equals zero vector, random vector, or  $\mathbf{f}_{d0}$ ;

$\mathbf{\Lambda}(t)$  represents the diagonal matrix of multiplication coefficient at time  $t$ ;

$\mathbf{\Lambda}_{ii}(t)$  represents the  $i$ -th principal diagonal element of  $\mathbf{\Lambda}(t)$ ;

$\text{diag}(\cdot)$  represents a diagonal matrix.

### 3.3 Loop Equation

According to Equations (2) and (3), the nonlinear loop equation of CIC can be described by the following mathematical equations:

$$\begin{aligned}
\mathbf{f}(t) &= \mathbf{f}(0) + \int_0^t \mathbf{\Lambda}(t) (\mathbf{f}_{d0} - \text{DE}(\text{EN}(\mathbf{f}(t)))) dt \\
\mathbf{f}(t) &= \mathbf{f}(0) + \int_0^t \mathbf{\Lambda}(t) (\mathbf{f}_{d0} - \text{NF}(\mathbf{f}(t))) dt
\end{aligned} \tag{4}$$

### 3.4 Nonlinear Function

The nonlinear function  $\text{NF}(\mathbf{f}(t))$  in Equation (4) can be expanded with the Taylor series at  $\mathbf{f}_0$  by the following mathematical expressions:

$$\begin{aligned}
\text{NF}(\mathbf{f}(t)) &= \text{NF}(\mathbf{f}_0) + \mathbf{o}(t) + \mathbf{O}(t) \\
\mathbf{o}_i(t) &= \sum_{j=1}^D (\mathbf{f}_j(t) - \mathbf{f}_{0j}) \left. \frac{\partial \text{NF}_i(\mathbf{f}(t))}{\partial \mathbf{f}_j(t)} \right|_{\mathbf{f}(t)=\mathbf{f}_0} , \\
\mathbf{o}(t), \mathbf{O}(t) &\in \mathbf{R}^D; i, j = 1, 2, \dots, D
\end{aligned} \tag{5}$$

where:

$\text{NF}(\mathbf{f}_0)$  denotes the constant term of  $\text{NF}(\mathbf{f}(t))$  at  $\mathbf{f}_0$ ;

$\mathbf{o}(t)$  denotes the first-order term of  $\text{NF}(\mathbf{f}(t))$  at time  $t$ ;  
 $\mathbf{O}(t)$  denotes the second-order and higher-order term of  $\text{NF}(\mathbf{f}(t))$  at time  $t$ ;  
 $\mathbf{o}_i(t)$  denotes the  $i$ -th element of  $\mathbf{o}(t)$ ;  
 $\mathbf{f}_j(t)$  denotes the  $j$ -th element of  $\mathbf{f}(t)$ ;  
 $\mathbf{f}_{0j}$  denotes the  $j$ -th element of  $\mathbf{f}_0$ ;  
 $\text{NF}_i(\mathbf{f}(t))$  denotes the  $i$ -th element of  $\text{NF}(\mathbf{f}(t))$ .

For the convenience of later theoretical analysis, after discarding the second-order and higher-order term  $\mathbf{O}(t)$ , the  $\text{NF}(\mathbf{f}(t))$  can be approximated by the following linear function:

$$\text{NF}(\mathbf{f}(t)) \approx \text{NF}(\mathbf{f}_0) + \mathbf{o}(t). \quad (6)$$

The linear term  $\mathbf{o}_i(t)$  can be further approximated by the following mathematical formulas:

$$\mathbf{o}_i(t) \approx (\mathbf{f}_i(t) - \mathbf{f}_{0i}) \left. \frac{\partial \text{NF}_i(\mathbf{f})}{\partial \mathbf{f}_i(t)} \right|_{\mathbf{f}_i(t)=\mathbf{f}_{0i}}. \quad (7)$$

$i = 1, 2, \dots, D$

According to Equation (7), the linear term  $\mathbf{o}(t)$  can be rewritten by the following equations:

$$\begin{aligned} \mathbf{o}(t) &\approx \mathbf{U}(t)(\mathbf{f}(t) - \mathbf{x}_0) \\ \mathbf{U}(t) &= \text{diag}(\mathbf{U}_{11}(t) \quad \mathbf{U}_{22}(t) \quad \dots \quad \mathbf{U}_{DD}(t)) \\ \mathbf{U}_{ii}(t) &= \left. \frac{\partial \text{NF}_i(\mathbf{f}(t))}{\partial \mathbf{f}_i(t)} \right|_{\mathbf{f}(t)=\mathbf{f}_0}, \\ \mathbf{U}(t) &\in \mathbb{R}^{D \times D}; i = 1, 2, \dots, D \end{aligned} \quad (8)$$

where:

$\mathbf{U}(t)$  is the coefficient matrix at time  $t$ ;  
 $\mathbf{U}_{ii}(t)$  is the  $i$ -th principal diagonal element of  $\mathbf{U}(t)$ .

### 3.5 Steady-State Error

The reconstruction error between the expected reconstruction image  $\mathbf{f}(t)$  and the original image  $\mathbf{f}_0$  can be described by the following mathematical equation:

$$\begin{aligned} \mathbf{r}(t) &= \mathbf{f}(t) - \mathbf{f}_0 \\ \mathbf{r}(t) &\in \mathbb{R}^D \end{aligned} \quad (9)$$

According to Equation (4), the expected reconstruction image  $\mathbf{f}(t)$  at time  $t+\Delta t$  can be expressed by the following mathematical equation:



$$\mathbf{f}(t+\Delta t) = \mathbf{f}(t) + \int_t^{t+\Delta t} \Lambda(t) (\mathbf{f}_{d0} - \mathbf{NF}(\mathbf{f}(t))) dt \quad (10)$$

s.t.  $\Delta t > 0$

Subtracting  $\mathbf{f}_0$  from both sides of Equation (10), the following mathematical equation can be obtained:

$$\mathbf{f}(t+\Delta t) - \mathbf{f}_0 = \mathbf{f}(t) - \mathbf{f}_0 + \int_t^{t+\Delta t} \Lambda(t) (\mathbf{f}_{d0} - \mathbf{NF}(\mathbf{f}(t))) dt \quad (11)$$

According to Equation (9), the following mathematical expressions can be gained:

$$\begin{aligned} \mathbf{r}(t+\Delta t) &= \mathbf{r}(t) + \int_t^{t+\Delta t} \Lambda(t) (\mathbf{f}_{d0} - \mathbf{NF}(\mathbf{f}(t))) dt \\ \mathbf{r}(t+\Delta t) &= \mathbf{f}(t+\Delta t) - \mathbf{f}_0 \end{aligned} \quad (12)$$

where  $\mathbf{r}(t+\Delta t)$  represents the error vector at time  $t+\Delta t$ .

If  $\Delta t$  is close to zero, Equation (12) can be approximated by the following mathematical formula:

$$\begin{aligned} \mathbf{r}(t+\Delta t) &\approx \mathbf{r}(t) + \Lambda(t) (\mathbf{f}_{d0} - \mathbf{NF}(\mathbf{f}(t))) \Delta t \\ &\text{s.t. } \Delta t \rightarrow 0 \end{aligned} \quad (13)$$

According to Equations (2), (6), (8), and (9), the following mathematical equations can be acquired:

$$\begin{aligned} \mathbf{r}(t+\Delta t) &\approx \mathbf{r}(t) - \Lambda(t) \mathbf{o}(t) \Delta t \\ &\approx \mathbf{r}(t) - \Lambda(t) \mathbf{U}(t) (\mathbf{f}(t) - \mathbf{f}_0) \Delta t \\ &= \mathbf{r}(t) - \Lambda(t) \mathbf{U}(t) \mathbf{r}(t) \Delta t \\ &= (\mathbf{I} - \Lambda(t) \mathbf{U}(t) \Delta t) \mathbf{r}(t) \\ &= (\mathbf{I} - \Delta t \Lambda(t) \mathbf{U}(t)) \mathbf{r}(t) \end{aligned} \quad (14)$$

where  $\mathbf{I}$  denotes the unit matrix.

Computing norm in both sides of Equation (14), the following mathematical inequation can be obtained:

$$\|\mathbf{r}(t+\Delta t)\|_2 \leq \|\mathbf{I} - \Delta t \Lambda(t) \mathbf{U}(t)\|_F \cdot \|\mathbf{r}(t)\|_2 \quad (15)$$

where:

subscript 2 means 2-norm;

subscript F means Frobenius-norm.

We can always choose suitable  $\Lambda(t)$  and  $\mathbf{U}(t)$  to satisfy the following inequality:

$$\|\mathbf{I} - \Delta t \Lambda(t) \mathbf{U}(t)\|_{\mathbb{F}} < 1, \quad (16)$$

For example,  $\Lambda(t)$  and  $\mathbf{U}(t)$  are respectively proportional to a unit matrix:

$$\begin{aligned} \Lambda(t) &= \eta \mathbf{I} \\ \mathbf{U}(t) &= \mu(t) \mathbf{I} \end{aligned} \quad (17)$$

$$\mu(t) = \frac{1}{D} \sum_{i=1}^D \mathbf{U}_{ii}(t) = \frac{1}{D} \sum_{i=1}^D \left. \frac{\partial \text{NF}_i(\mathbf{f}(t))}{\partial \mathbf{f}_i(t)} \right|_{\mathbf{f}(t)=\mathbf{f}_0}$$

where:

$\eta$  is a constant;

$\mu(t)$  is the average of  $\mathbf{U}_{ii}(t)$  in Equation (8).

According to Equation (17), we can always find a proper  $\eta$  to meet Inequation (16):

$$\begin{aligned} \|\mathbf{I} - \Delta t \Lambda(t) \mathbf{U}(t)\|_{\mathbb{F}} &= \|\mathbf{I} - \Delta t \cdot \eta \mathbf{I} \cdot \mu(t) \mathbf{I}\|_{\mathbb{F}} = \|(1 - \Delta t \cdot \eta \cdot \mu(t)) \mathbf{I}\|_{\mathbb{F}} \\ &= |1 - \Delta t \cdot \mu(t) \cdot \eta| \cdot \|\mathbf{I}\|_{\mathbb{F}} = |1 - \Delta t \cdot \mu(t) \cdot \eta| \cdot \sqrt{D} < 1 \end{aligned} \quad (18)$$

$$\Rightarrow \begin{cases} \frac{1 - \frac{1}{\sqrt{D}}}{\Delta t \cdot \mu(t)} < \eta < \frac{1 + \frac{1}{\sqrt{D}}}{\Delta t \cdot \mu(t)}, \mu(t) > 0 \\ \frac{1 + \frac{1}{\sqrt{D}}}{\Delta t \cdot \mu(t)} < \eta < \frac{1 - \frac{1}{\sqrt{D}}}{\Delta t \cdot \mu(t)}, \mu(t) < 0 \end{cases}$$

According to Equations (15) and (16), the following mathematical inequality can be obtained:

$$\|\mathbf{r}(t + \Delta t)\|_2 < \|\mathbf{r}(t)\|_2. \quad (19)$$

According to Inequation (19), if time  $t$  is close to infinite in steady-state, the reconstruction error approximates to zero, and  $\mathbf{f}(t)$  approximates to  $\mathbf{f}_0$ . It can be depicted by the following mathematical limit:

$$\begin{aligned} \lim_{t \rightarrow \infty} \mathbf{r}(t) &= \lim_{t \rightarrow \infty} (\mathbf{f}(t) - \mathbf{f}_0) = 0 \\ \lim_{t \rightarrow \infty} \mathbf{f}(t) &= \mathbf{f}_0 \end{aligned} \quad (20)$$

Therefore, the proposed CIC can achieve the perfect reconstruction image  $\mathbf{f}(t)$  which is close to the original image  $\mathbf{f}_0$ .

### 3.6 Algorithm Description

The proposed CIC algorithm is described in Figure 3, where  $N$  is the total number of iterations.

**Algorithm: CIC**  
**Input:**  $f_0$   
**Initialization:**  
 $n = 1, f_{d0} = NF(f_0), f = 0, f_{d0},$  or random vector  
**while**  $n \leq N$   
    **update**  $f$  according to equation (4), (6), (11) and (17)  
     $n = n+1$   
**end**  
**Output:**  $f$

Figure 2. CIC algorithm description.

## 4 Experiment

### 4.1 Experimental Conditions

Five public image compression datasets, Kodak, CLIC2021 Test, CLIC2021 Validation, CLIC2022 Validation, and CLIC2024 Validation, are utilized to evaluate the performance of LIC methods. These image datasets are enumerated in Table 2 including the total number of images, the resolution of images, and the web link of image dataset.

Table 2. Image datasets.

| Dataset             | Detail     |   |
|---------------------|------------|---|
| Kodak               | Number     | 24  |
|                     | Resolution | $768 \times 512$  |
|                     | Link       | <a href="https://www.kaggle.com/datasets/sherylmehta/kodak-dataset">https://www.kaggle.com/datasets/sherylmehta/kodak-dataset</a> |
| CLIC2021 Test       | Number     | 60  |
|                     | Resolution | $751 \times 500 \sim 2048 \times 1400$  |
|                     | Link       | <a href="https://clic.compression.cc/2021/tasks/index.html">https://clic.compression.cc/2021/tasks/index.html</a>                 |
| CLIC2021 Validation | Number     | 41  |
|                     | Resolution | $512 \times 384 \sim 2048 \times 1370$  |
|                     | Link       | <a href="https://clic.compression.cc/2021/tasks/index.html">https://clic.compression.cc/2021/tasks/index.html</a>                 |
| CLIC2022 Validation | Number     | 30  |
|                     | Resolution | $1151 \times 2048 \sim 2048 \times 2048$  |
|                     | Link       | <a href="https://clic.compression.cc/2022/">https://clic.compression.cc/2022/</a>   |
| CLIC2024 Validation | Number     | 30  |
|                     | Resolution | $1152 \times 2048 \sim 2048 \times 2048$  |

|  |      |   |
|--|------|---|
|  | Link | <a href="https://compression.cc/tasks/">https://compression.cc/tasks/</a> |
|--|------|---|

Five open-source competing methods, Deep Lossy Plus Residual Coding (DLPR) [19], Conditional Diffusion Compression (CDC) [20], Image Compression with Transformers (ICT) [21], Quantized ResNet VAE (QRVAE) [27], and Vector Quantized VAE (VQVAE) [28], are adopted for comparison with the proposed CIC method. These methods are listed in Table 3 including algorithm name and web link. Because the proposed CIC method has the property of plug-and-play and Post-Training, five CIC versions of the competing methods, circular DLPR (CDLPR), circular CDC (CCDC), circular ICT (CICT), circular QRVAE (CQRVAE), and circular VQVAE (CVQVAE), are presented for comparison.

**Table 3. Competing methods.**

| Method | Link  |
|--------|---|
| DLPR   | <a href="https://github.com/BYchao100/Deep-Lossy-Plus-Residual-Coding">https://github.com/BYchao100/Deep-Lossy-Plus-Residual-Coding</a>   |
| CDC    | <a href="https://github.com/buggyang/CDC_compression">https://github.com/buggyang/CDC_compression</a>   |
| ICT    | <a href="https://github.com/BYchao100/Towards-Image-Compression-and-Analysis-with-Transformers">https://github.com/BYchao100/Towards-Image-Compression-and-Analysis-with-Transformers</a> |
| QRVAE  | <a href="https://github.com/duanzhihao/qres-vae">https://github.com/duanzhihao/qres-vae</a>   |
| VQVAE  | <a href="https://github.com/TimeEscaper/vq-vic">https://github.com/TimeEscaper/vq-vic</a>   |

Three experiments, quantization parameter, reconstruction performance, and out-of-sample, are designed to compare the performance between the conventional SIC and the proposed CIC.

Three performance metrics, PSNR, SSIM, and BPSP, are selected to assess the capability of SIC and CIC. For reconstruction image  $\mathbf{f}$  and original image  $\mathbf{f}_0$ , the definitions of PSNR, SSIM, and BPSP are described by the following mathematical equations:

$$\text{PSNR}(\mathbf{f}, \mathbf{f}_0) = 10 \lg \left( \frac{255^2}{\frac{1}{D} \sum_{i=1}^D (\mathbf{f}_i - \mathbf{f}_{0i})^2} \right), \quad (21)$$

$$\text{SSIM}(\mathbf{f}, \mathbf{f}_0) = \frac{(2\mu_{\mathbf{f}}\mu_{\mathbf{f}_0} + (0.01 \times 255)^2)(2\sigma_{\mathbf{f}\mathbf{f}_0} + (0.03 \times 255)^2)}{(\mu_{\mathbf{f}}^2 + \mu_{\mathbf{f}_0}^2 + (0.01 \times 255)^2)(\sigma_{\mathbf{f}}^2 + \sigma_{\mathbf{f}_0}^2 + (0.03 \times 255)^2)}, \quad (22)$$

$$\text{BPSP} = \frac{B}{S \times W \times H \times C}, \quad (23)$$

where:

$\mathbf{f}_i$  is the  $i$ -th element of  $\mathbf{f}$ ;

$\mathbf{f}_{0i}$  is the  $i$ -th element of  $\mathbf{f}_0$ ;

$\mu_f$  is the element-wised mean of  $\mathbf{f}$ ;  
 $\mu_{f_0}$  is the element-wised mean of  $\mathbf{f}_0$ ;  
 $\sigma_f$  is the element-wised standard deviation of  $\mathbf{f}$ ;  
 $\sigma_{f_0}$  is the element-wised standard deviation of  $\mathbf{f}_0$ ;  
 $\sigma_{ff_0}$  is the element-wised covariance of  $\mathbf{f}$  and  $\mathbf{f}_0$ ;  
 $B$  is the total number of bits for an image;  
 $S$  is the total number of bits for a subpixel;  
 $W$  is the width of an image;  
 $H$  is the height of an image;  
 $C$  is the total number of channels of an image.

For the purpose of comparing the difference between the reconstruction images of SIC and CIC, absolute difference image and logic difference image are defined by the following mathematical equations.

$$\begin{aligned}
 \mathbf{f}_a(i, j) &= |\mathbf{f}_t(i, j) - \mathbf{f}_r(i, j)| \\
 \mathbf{f}_l(i, j) &= \begin{cases} 1, & |\mathbf{f}_t(i, j) - \mathbf{f}_r(i, j)| > T \\ 0, & |\mathbf{f}_t(i, j) - \mathbf{f}_r(i, j)| \leq T \end{cases}, \\
 \mathbf{f}_a, \mathbf{f}_l, \mathbf{f}_t, \mathbf{f}_r &\in \mathbb{R}^{H \times W}; i, j \in \mathbb{Z}; T \in \mathbb{R}
 \end{aligned} \tag{24}$$

where:

$\mathbf{f}_a$  is the absolute difference image;  
 $\mathbf{f}_l$  is the logic difference image;  
 $\mathbf{f}$  is the testing image;  
 $\mathbf{f}_r$  is the reference image;  
 $i$  is the row index of an image;  
 $j$  is the column index of an image;  
 $H$  is the row size of an image;  
 $W$  is the column size of an image;  
 $T$  is a threshold.

The experimental hardware platforms contain Intel CPU and Nvidia GPU. The experimental software platforms contain Google TensorFlow, FaceBook PyTorch, Microsoft COLAB, and MathWorks MATLAB running on Windows or Linux operating systems. Detailed hardware and software configurations are listed in Table 4.

**Table 4. Detailed hardware and software configurations.**

| Hardware Configurations |                   |
|-------------------------|-------------------|
| Item                    | Value             |
| CPU Type                | Intel Core i7     |
| CPU Memory              | 8GB               |
| GPU Type                | NVIDIA Tesla V100 |
| GPU Memory              | 16GB              |

| Software Configurations       |       |
|-------------------------------|-------|
| Item                          | Value |
| Input/Output Channels         | 3/3   |
| Batch Size                    | 1     |
| Block Size                    | 64×64 |
| Iteration Number (N)          | 1~10  |
| Iteration Constant ( $\eta$ ) | -1~+1 |

## 4.2 Experimental Results

### 4.2.1 Experimental Results of Quantization Parameter

This experiment is designed to investigate the relationship between the performance of image compression and the quantization parameter. This experiment focuses on the DLPR and CDLPR algorithms and the single image, kodim01.png, of Kodak image dataset. It is shown in Figure 3 that PSNR decreases while quantization parameter  $\tau$  increases and CDLPR outperforms DLPR in PSNR. It is also displayed in Figure 4 that SSIM decreases while quantization parameter  $\tau$  increases and CDLPR exceeds DLPR in SSIM. It is further illustrated in Figure 5 that BPSP decreases while quantization parameter  $\tau$  increases and CDLPR surpasses DLPR in BPSP.

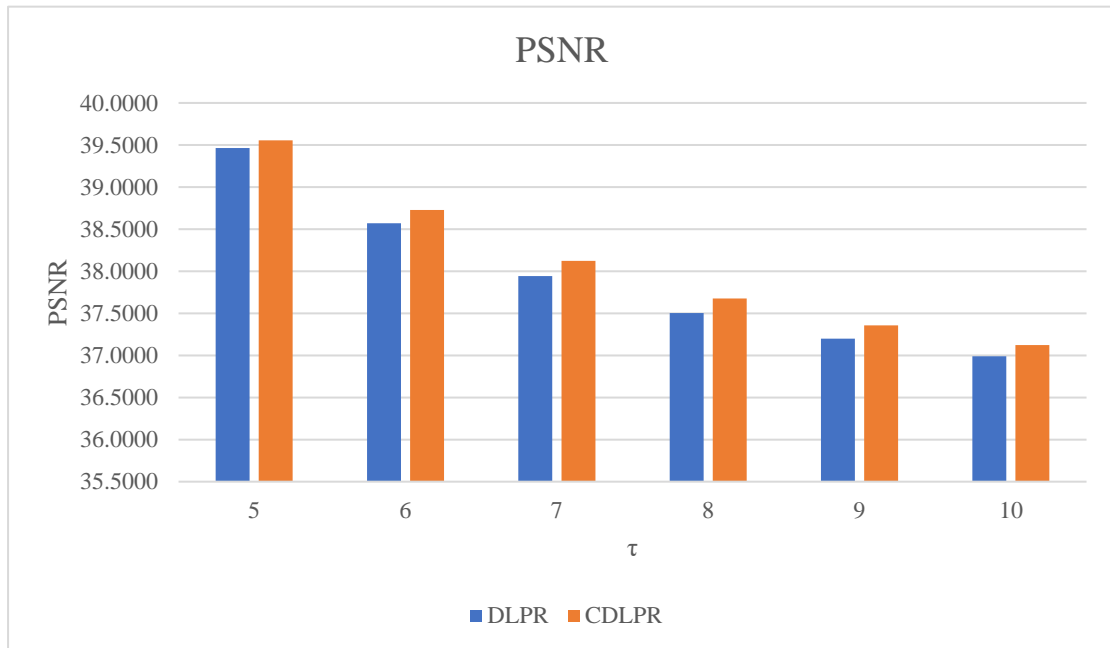


**Figure 3. PSNR of DLPR and CDLPR on single image of Kodak image dataset.**

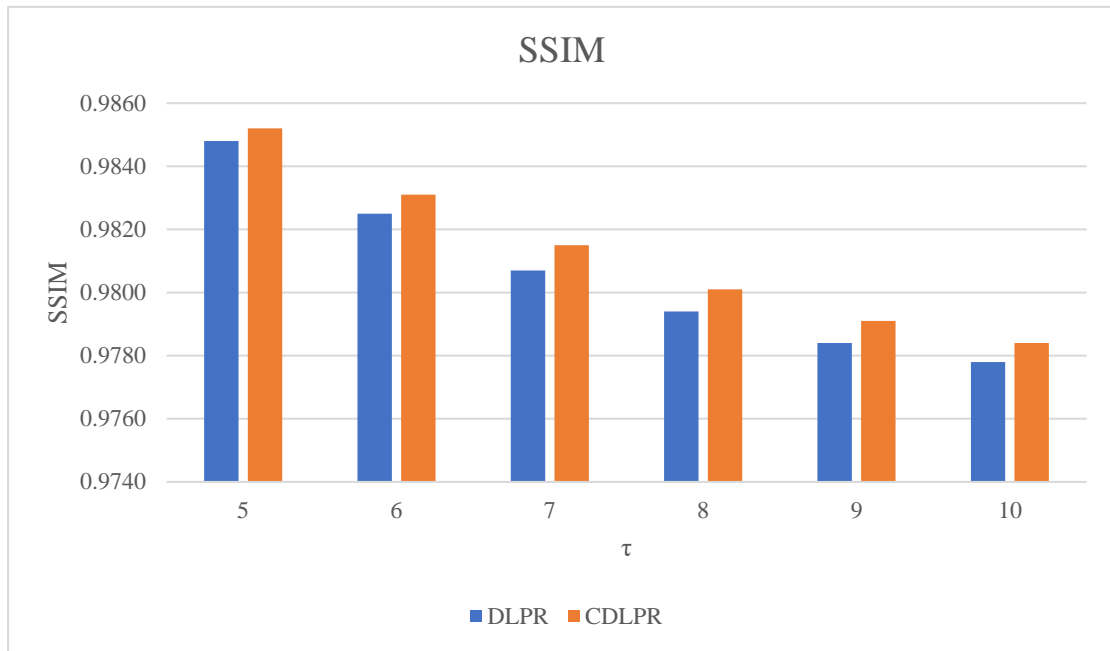


**Figure 4. SSIM of DLPR and CDLPR on single image of Kodak image dataset.**

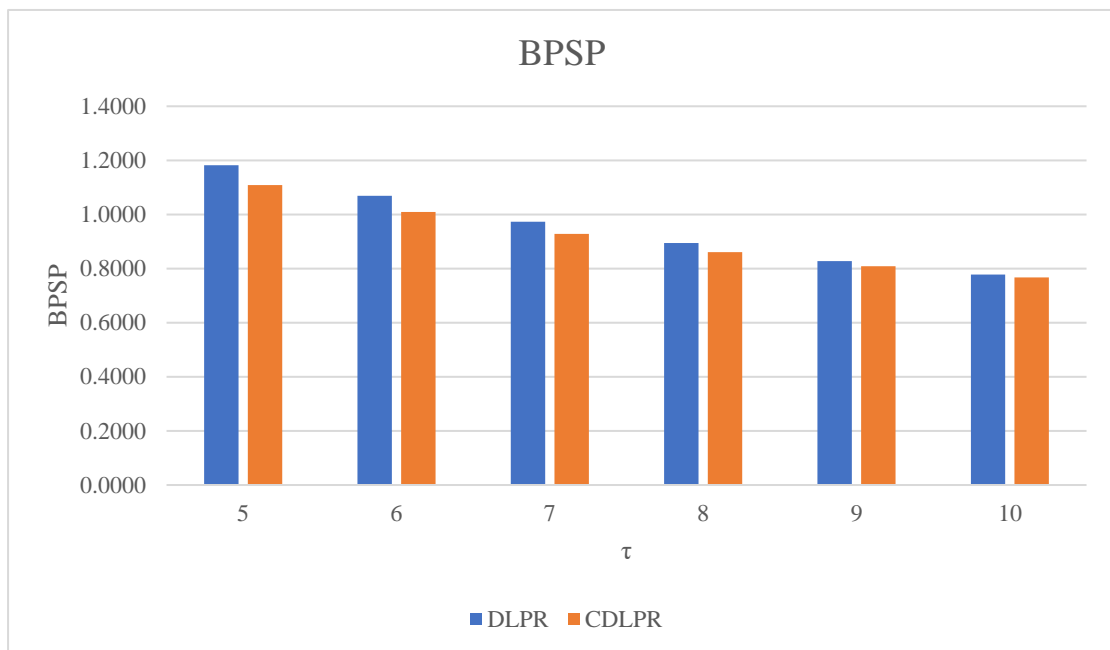


**Figure 5. BPSP of DLPR and CDLPR on single image of Kodak image dataset.**

#### 4.2.2 Experimental Results of Reconstruction Performance

This experiment is planned to compare the reconstruction performance between the traditional SIC and the proposed CIC. This experiment concentrates on five open-source competing methods and five public image datasets.

Figures 6, 7, and 8 demonstrate the PSNR, SSIM, and BPSP of DLPR and CDLPR algorithms with quantization parameter  $\tau=7$  on Kodak image dataset. The experimental results indicate that the proposed CDLPR is superior to the classical DLPR in PSNR, SSIM, and BPSP.

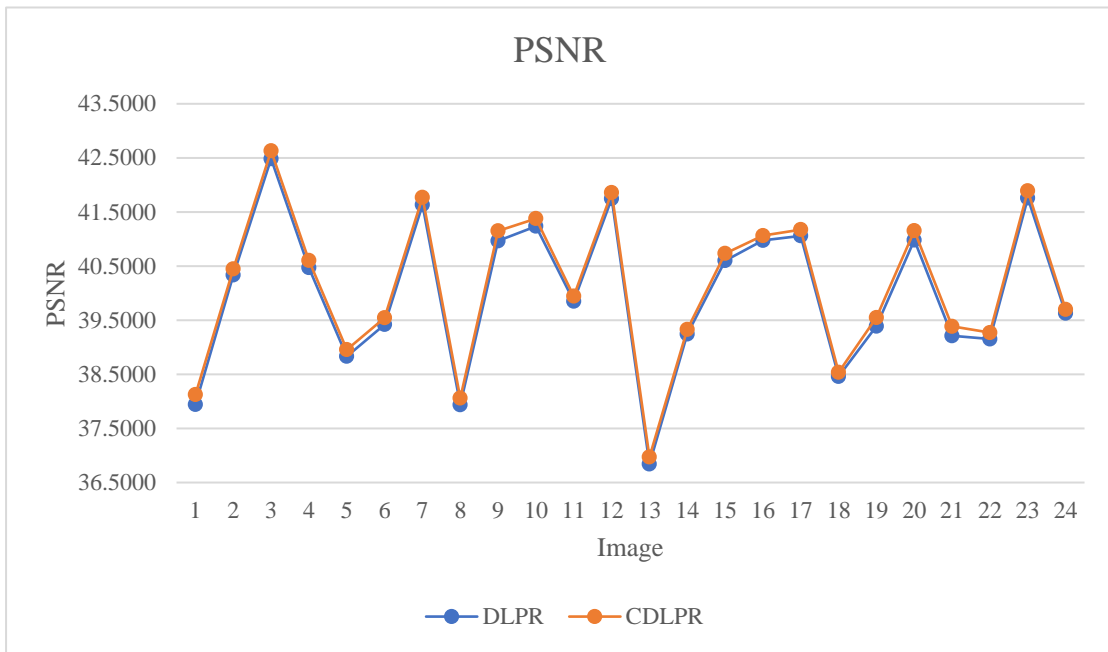


**Figure 6. PSNR of DLPR and CDLPR on Kodak image dataset.**

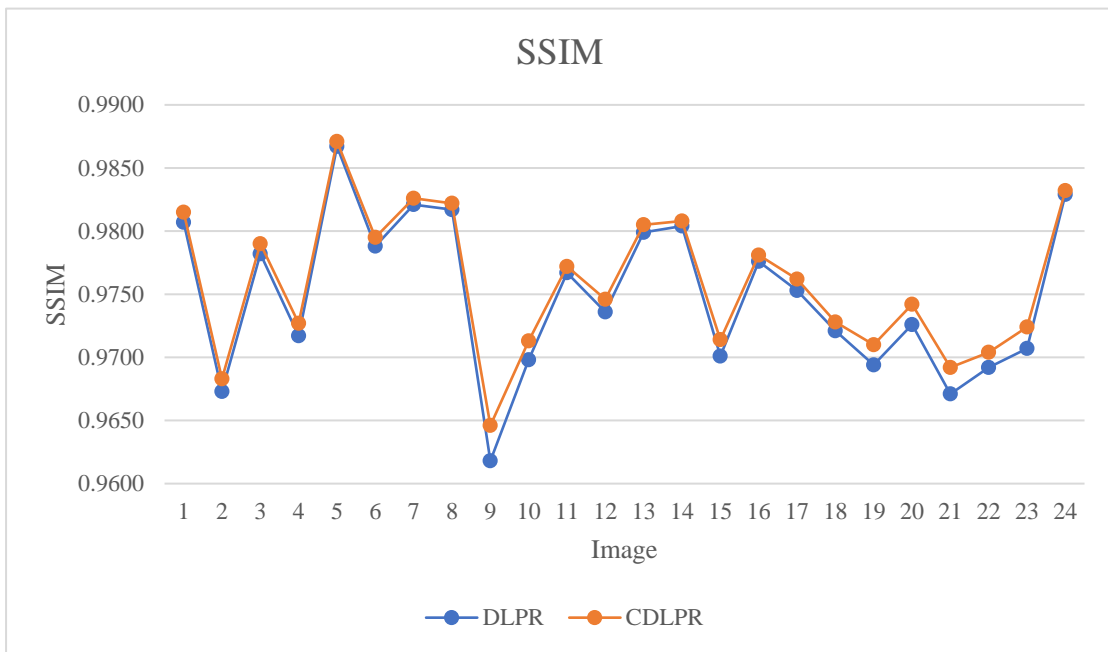


**Figure 7. SSIM of DLPR and CDLPR on Kodak image dataset.**



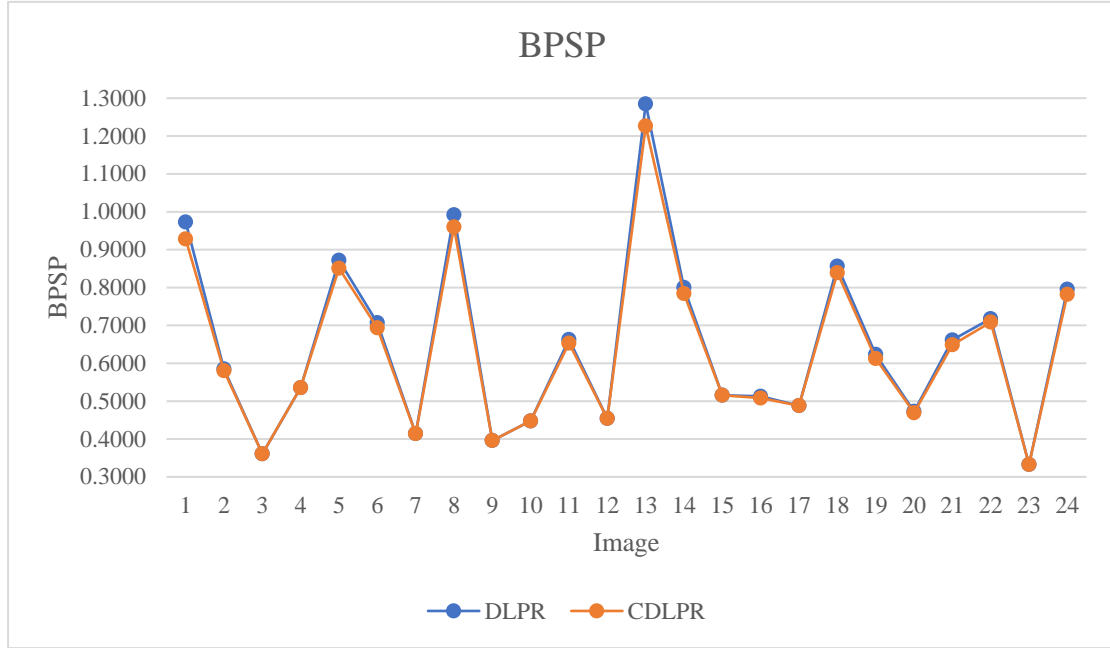


**Figure 8. BPSD of DLPR and CDLPR on Kodak image dataset.**

Table 5 shows the PSNR, SSIM, and BPSD of DLPR and CDLPR with quantization parameter  $\tau=7$  on five image datasets. The PSNR, SSIM, and BPSD are the averages on each dataset.  $\Delta$  is the average increment of PSNR or SSIM between CDLPR and DLPR on each dataset.  $\Delta_m$  is the maximum increment of PSNR or SSIM between CDLPR and DLPR on each dataset.  $\Delta$  is also the average decrement of BPSD between CDLPR and DLPR on each dataset.  $\Delta_m$  is also the maximum decrement of BPSD between CDLPR and DLPR on each dataset. The maximum PSNR increment is 1.7142 dB on CLIC2021 Test image dataset. The experimental results manifest that the proposed CDLPR holds superiority over the classical DLPR in PSNR, SSIM, and BPSD.

Table 6 displays the PSNR, SSIM, and BPSD of CDC and CCDC with quantization parameter 0.0128 on five image datasets. The maximum PSNR increment is 5.7129 dB on CLIC2021 Test image dataset. For the convenience of computation, some images are clipped to the same size as images of Kodak image dataset. The experimental results reveal that the proposed CCDC overbalances the classical CDC in PSNR and SSIM while both of them have the same BPSD.

Table 7 illustrates the PSNR, SSIM, and BPSD of ICT and CICT with quantization parameter 3 on five image datasets. The maximum PSNR increment is 2.7907 dB on CLIC2021 Test image dataset. For the expediency of calculation, some images are trimmed to the same size as images of Kodak image dataset. The experimental results uncover that the proposed CICT overmatches the classical ICT in PSNR, SSIM, and BPSD.

Table 8 demonstrates the PSNR, SSIM, and BPSD of QRVAE and CQRVAE with quantization parameter 16 on five image datasets. The maximum PSNR increment is 4.9347 dB on CLIC2021 Test image dataset. For the facilitation of implementation, some images are tailored to the same size of images of Kodak image dataset. The experimental results indicate that the proposed CQRVAE outperforms the classical QRVAE in PSNR and SSIM while both of them have the same BPSD.

Table 9 exhibits the PSNR, SSIM, and BPSP of VQVAE and CVQVAE on five image datasets. The maximum PSNR increment is 1.5219 dB on CLIC2021 Validation image dataset. For the easiness of realization, some images are cropped to the same size as images of Kodak image dataset. The experimental results make clear that the proposed CVQVAE surpasses the classical VQVAE in PSNR and SSIM while both of them have the same BPSP.

**Table 5. Experimental results of DLPR and CDLPR on five image datasets.**

| Dataset |            | Kodak   | CLIC2021<br>Test | CLIC2021<br>Validation | CLIC2022<br>Validation | CLIC2024<br>Validation |
|---------|------------|---------|------------------|------------------------|------------------------|------------------------|
| PSNR↑   | DLPR       | 40.0063 | 41.3359          | 40.5765                | 41.0578                | 40.2871                |
|         | CDLPR      | 40.1345 | 41.5588          | 40.7525                | 41.2347                | 40.4597                |
|         | $\Delta$   | 0.1282  | 0.2229           | 0.1760                 | 0.1769                 | 0.1726                 |
|         | $\Delta_m$ | 0.1861  | <b>1.7142</b>    | 0.4736                 | 0.3763                 | 0.3537                 |
| SSIM↑   | DLPR       | 0.9749  | 0.9711           | 0.9668                 | 0.9714                 | 0.9702                 |
|         | CDLPR      | 0.9759  | 0.9739           | 0.9689                 | 0.9728                 | 0.9722                 |
|         | $\Delta$   | 0.0010  | 0.0027           | 0.0021                 | 0.0014                 | 0.0019                 |
|         | $\Delta_m$ | 0.0028  | 0.0388           | 0.0129                 | 0.0054                 | 0.0110                 |
| BPSP↓   | DLPR       | 0.6443  | 0.4610           | 0.5089                 | 0.5436                 | 0.5920                 |
|         | CDLPR      | 0.6329  | 0.4541           | 0.4999                 | 0.5312                 | 0.5802                 |
|         | $\Delta$   | 0.0114  | 0.0069           | 0.0090                 | 0.0123                 | 0.0119                 |
|         | $\Delta_m$ | 0.0585  | 0.0565           | 0.0577                 | 0.0803                 | 0.0522                 |

**Table 6. Experimental results of CDC and CCDC on five image datasets.**

| Dataset |            | Kodak   | CLIC2021<br>Test | CLIC2021<br>Validation | CLIC2022<br>Validation | CLIC2024<br>Validation |
|---------|------------|---------|------------------|------------------------|------------------------|------------------------|
| PSNR↑   | CDC        | 34.3532 | 38.2491          | 36.8646                | 37.0497                | 36.7745                |
|         | CCDC       | 34.4227 | 38.7852          | 37.0708                | 37.6947                | 37.0449                |
|         | $\Delta$   | 0.0694  | 0.5361           | 0.2062                 | 0.6450                 | 0.2704                 |
|         | $\Delta_m$ | 0.1448  | <b>5.7129</b>    | 1.8855                 | 2.8527                 | 2.8118                 |
| SSIM↑   | CDC        | 0.9379  | 0.9447           | 0.9364                 | 0.9409                 | 0.9387                 |
|         | CCDC       | 0.9382  | 0.9466           | 0.9373                 | 0.9417                 | 0.9405                 |
|         | $\Delta$   | 0.0003  | 0.0019           | 0.0009                 | 0.0008                 | 0.0018                 |
|         | $\Delta_m$ | 0.0015  | 0.0503           | 0.0144                 | 0.0095                 | 0.0131                 |
| BPSP↓   | CDC        | 0.8389  | 0.3926           | 0.5368                 | 0.4751                 | 0.4815                 |
|         | CCDC       | 0.8389  | 0.3926           | 0.5368                 | 0.4751                 | 0.4815                 |
|         | $\Delta$   | 0.0000  | 0.0000           | 0.0000                 | 0.0000                 | 0.0000                 |
|         | $\Delta_m$ | 0.0000  | 0.0000           | 0.0000                 | 0.0000                 | 0.0000                 |

**Table 7. Experimental results of ICT and CICT on five image datasets.**

| Dataset |     | Kodak   | CLIC2021<br>Test | CLIC2021<br>Validation | CLIC2022<br>Validation | CLIC2024<br>Validation |
|---------|-----|---------|------------------|------------------------|------------------------|------------------------|
| PSNR↑   | ICT | 29.4609 | 29.1243          | 29.6862                | 29.3554                | 28.1825                |

|                   |            |         |               |         |         |         |
|-------------------|------------|---------|---------------|---------|---------|---------|
|                   | CICT       | 29.5614 | 29.2873       | 29.7799 | 29.4643 | 28.2794 |
|                   | $\Delta$   | 0.1005  | 0.1630        | 0.0936  | 0.1089  | 0.0969  |
|                   | $\Delta_m$ | 0.2573  | <b>2.7907</b> | 0.2281  | 0.2830  | 0.2254  |
| SSIM $\uparrow$   | ICT        | 0.7191  | 0.7994        | 0.7812  | 0.7940  | 0.7931  |
|                   | CICT       | 0.7254  | 0.8042        | 0.7856  | 0.7984  | 0.7979  |
|                   | $\Delta$   | 0.0062  | 0.0048        | 0.0045  | 0.0045  | 0.0048  |
|                   | $\Delta_m$ | 0.0112  | 0.0237        | 0.0107  | 0.0142  | 0.0305  |
| BPSP $\downarrow$ | ICT        | 0.4007  | 0.3947        | 0.3445  | 0.4665  | 0.5397  |
|                   | CICT       | 0.3313  | 0.3891        | 0.3395  | 0.4058  | 0.4683  |
|                   | $\Delta$   | 0.0694  | 0.0056        | 0.0049  | 0.0607  | 0.0715  |
|                   | $\Delta_m$ | 0.1378  | 0.0976        | 0.1155  | 0.1097  | 0.1148  |

**Table 8. Experimental results of QRVAE and CQRVAE on five image datasets.**

| Dataset           |            | Kodak   | CLIC2021<br>Test | CLIC2021<br>Validation | CLIC2022<br>Validation | CLIC2024<br>Validation |
|-------------------|------------|---------|------------------|------------------------|------------------------|------------------------|
| PSNR $\uparrow$   | QRVAE      | 30.0170 | 34.0337          | 32.3537                | 33.4110                | 32.6968                |
|                   | CQRVAE     | 30.9856 | 35.2369          | 33.3826                | 34.4798                | 33.8661                |
|                   | $\Delta$   | 0.9686  | 1.2032           | 1.0289                 | 1.0688                 | 1.1693                 |
|                   | $\Delta_m$ | 1.2953  | <b>4.9347</b>    | 2.5864                 | 4.3077                 | 3.6048                 |
| SSIM $\uparrow$   | QRVAE      | 0.8093  | 0.8937           | 0.8625                 | 0.8856                 | 0.8873                 |
|                   | CQRVAE     | 0.8599  | 0.9102           | 0.8887                 | 0.9013                 | 0.9050                 |
|                   | $\Delta$   | 0.0506  | 0.0164           | 0.0262                 | 0.0157                 | 0.0177                 |
|                   | $\Delta_m$ | 0.0966  | 0.0991           | 0.1094                 | 0.1028                 | 0.0533                 |
| BPSP $\downarrow$ | QRVAE      | 0.1829  | 0.0653           | 0.1008                 | 0.0948                 | 0.0860                 |
|                   | CQRVAE     | 0.1829  | 0.0653           | 0.1008                 | 0.0948                 | 0.0860                 |
|                   | $\Delta$   | 0.0000  | 0.0000           | 0.0000                 | 0.0000                 | 0.0000                 |
|                   | $\Delta_m$ | 0.0000  | 0.0000           | 0.0000                 | 0.0000                 | 0.0000                 |

**Table 9. Experimental results of VQVAE and CVQVAE on five image datasets.**

| Dataset           |            | Kodak   | CLIC2021<br>Test | CLIC2021<br>Validation | CLIC2022<br>Validation | CLIC2024<br>Validation |
|-------------------|------------|---------|------------------|------------------------|------------------------|------------------------|
| PSNR $\uparrow$   | VQVAE      | 32.1650 | 32.5532          | 32.8301                | 32.6257                | 33.1952                |
|                   | CVQVAE     | 32.5840 | 32.9286          | 33.2335                | 32.9414                | 33.5463                |
|                   | $\Delta$   | 0.4190  | 0.3755           | 0.4034                 | 0.3157                 | 0.3511                 |
|                   | $\Delta_m$ | 1.1633  | 0.8489           | <b>1.5219</b>          | 1.2535                 | 0.8269                 |
| SSIM $\uparrow$   | VQVAE      | 0.9657  | 0.9613           | 0.9578                 | 0.9685                 | 0.9576                 |
|                   | CVQVAE     | 0.9663  | 0.9626           | 0.9586                 | 0.9690                 | 0.9601                 |
|                   | $\Delta$   | 0.0006  | 0.0013           | 0.0009                 | 0.0005                 | 0.0025                 |
|                   | $\Delta_m$ | 0.0020  | 0.0195           | 0.0082                 | 0.0021                 | 0.0397                 |
| BPSP $\downarrow$ | VQVAE      | 0.9936  | 0.6831           | 0.7546                 | 0.7986                 | 0.8077                 |
|                   | CVQVAE     | 0.9936  | 0.6831           | 0.7546                 | 0.7986                 | 0.8077                 |
|                   | $\Delta$   | 0.0000  | 0.0000           | 0.0000                 | 0.0000                 | 0.0000                 |
|                   | $\Delta_m$ | 0.0000  | 0.0000           | 0.0000                 | 0.0000                 | 0.0000                 |

In order to explicitly show the performance difference of image reconstruction between the proposed CIC and the classical SIC, some example images are displayed in Figures 9 to 13.

Figure 9 shows the experimental results of DLPR and CDLPR with maximum PSNR increment on Kodak image dataset. Figure 9(a) is the original image, Figure 9(b) is the reconstruction image of DLPR, and Figure 9(c) is the reconstruction image of CDLPR. It is hard to discover the difference between Figure 9(b) and Figure 9(c). Figure 9(d) is the subblock of Figure 9(a), Figure 9(e) is the related subblock of Figure 9(b), and Figure 9(f) is the related subblock of Figure 9(c). Figure 9(d), (e), and (f) are marked with red boxes in Figure 9(a), (b), and (c) respectively. It is also hard to discover the difference between Figure 9(e) and Figure 9(f). Figure 9(g) is the absolute difference image block between Figure 9(e) and Figure 9(d), and Figure 9(h) is the absolute difference image block between Figure 9(f) and Figure 9(d). It is still hard to discover the difference between Figure 9(g) and Figure 9(h). Figure 9(i) is the logic difference image block between Figure 9(e) and Figure 9(d), and Figure 9(j) is the logic difference image block between Figure 9(f) and Figure 9(d). It is easy to discover the difference between Figure 9(i) and Figure 9(j). Figure 9(i) and Figure 9(j) indicate that the reconstruction image quality of CDLPR outperforms that of DLPR. Figure 9 indicates that the proposed method is effective for testing images with sharp edges.

Figure 10 displays the experimental results of DLPR and CDLPR with maximum PSNR rise on CLIC2021 test image dataset. Figure 10(a) is the original image, Figure 10(b) is the restoration image of DLPR, and Figure 10(c) is the restoration image of CDLPR. It is difficult to seek out the discrepancy between Figure 10(b) and Figure 10(c). Figure 10(d) is the subblock of Figure 10(a), Figure 10(e) is the related subblock of Figure 10(b), and Figure 10(f) is the related subblock of Figure 10(c). Figure 10(d), (e), and (f) are marked with red boxes in Figure 10(a), (b), and (c) respectively. It is also difficult to seek out the discrepancy between Figure 10(e) and Figure 10(f). Figure 10(g) is the absolute difference image block between Figure 10(e) and Figure 10(d), and Figure 10(h) is the absolute difference image block between Figure 10(f) and Figure 10(d). It is still difficult to seek out the discrepancy between Figure 10(g) and Figure 10(h). Figure 10(i) is the logic difference image block between Figure 10(e) and Figure 10(d), and Figure 10(j) is the logic difference image block between Figure 10(f) and Figure 10(d). It is effortless to seek out the discrepancy between Figure 10(i) and Figure 10(j). Figure 10(i) and Figure 10(j) reveal that the restoration image quality of CDLPR outbalances that of DLPR. Figure 10 shows that the proposed method is propitious to testing images with dark and high contrast.

Figure 11 illustrates the experimental results of DLPR and CDLPR with maximum PSNR increase on CLIC2021 validation image dataset. Figure 11(a) is the original image, Figure 11(b) is the recovery image of DLPR, and Figure 11(c) is the recovery image of CDLPR. It is tough to check the discrimination between Figure 11(b) and Figure 11(c). Figure 11(d) is the subblock of Figure 11(a), Figure 11(e) is the related subblock of Figure 11(b), and Figure 11(f) is the related subblock of Figure 11(c). Figure 11(d), (e), and (f) are marked with red boxes in Figure 11(a), (b), and (c) respectively. It is also tough to check the discrimination between Figure 11(e) and Figure 11(f). Figure 11(g) is the absolute difference image block between Figure 11(e) and Figure 11(d), and Figure 11(h) is the absolute difference image block between Figure 11(f) and Figure 11(d). It is still

tough to check the discrimination between Figure 11(g) and Figure 11(h). Figure 11(i) is the logic difference image block between Figure 11(e) and Figure 11(d), and Figure 11(j) is the logic difference image block between Figure 11(f) and Figure 11(d). It is toil-less to check the discrimination between Figure 11(i) and Figure 11(j). Figure 11(i) and Figure 11(j) uncover that the recovery image quality of CDLPR overmatches that of DLPR. Figure 11 demonstrates that the proposed method is appropriate for testing images with grid shapes.

Figure 12 demonstrates the experimental results of DLPR and CDLPR with maximum PSNR improvement on CLIC2022 validation image dataset. Figure 12(a) is the original image, Figure 12(b) is the reestablishment image of DLPR, and Figure 12(c) is the reestablishment image of CDLPR. It is arduous to examine the distinction between Figure 12(b) and Figure 12(c). Figure 12(d) is the subblock of Figure 12(a), Figure 12(e) is the related subblock of Figure 12(b), and Figure 12(f) is the related subblock of Figure 12(c). Figure 12(d), (e), and (f) are marked with red boxes in Figure 12(a), (b), and (c) respectively. It is also arduous to examine the distinction between Figure 12(e) and Figure 12(f). Figure 12(g) is the absolute difference image block between Figure 12(e) and Figure 12(d), and Figure 12(h) is the absolute difference image block between Figure 12(f) and Figure 12(d). It is still arduous to examine the distinction between Figure 12(g) and Figure 12(h). Figure 12(i) is the logic difference image block between Figure 12(e) and Figure 12(d), and Figure 12(j) is the logic difference image block between Figure 12(f) and Figure 12(d). It is convenient to examine the distinction between Figure 12(i) and Figure 12(j). Figure 12(i) and Figure 12(j) disclose that the reestablishment image quality of CDLPR exceeds that of DLPR. Figure 12 indicates that the proposed method is fit for testing images with dark backgrounds and high contrast.

Figure 13 exhibits the experimental results of DLPR and CDLPR with maximum PSNR gain on CLIC2024 validation image dataset. Figure 13(a) is the original image, Figure 13(b) is the rebuilding image of DLPR, and Figure 13(c) is the rebuilding image of CDLPR. It is formidable to inspect the distinguishing between Figure 13(b) and Figure 13(c). Figure 13(d) is the subblock of Figure 13(a), Figure 13(e) is the related subblock of Figure 13(b), and Figure 13(f) is the related subblock of Figure 13(c). Figure 13(d), (e), and (f) are marked with red boxes in Figure 13(a), (b), and (c) respectively. It is also formidable to inspect the distinguishing between Figure 13(e) and Figure 13(f). Figure 13(g) is the absolute difference image block between Figure 13(e) and Figure 13(d), and Figure 13(h) is the absolute difference image block between Figure 13(f) and Figure 13(d). It is still formidable to inspect the distinguishing between Figure 13(g) and Figure 13(h). Figure 13(i) is the logic difference image block between Figure 13(e) and Figure 13(d), and Figure 13(j) is the logic difference image block between Figure 13(f) and Figure 13(d). It is facile to inspect the distinguishing between Figure 13(i) and Figure 13(j). Figure 13(i) and Figure 13(j) expose that the rebuilding image quality of CDLPR surpasses that of DLPR. Figure 13 shows the proposed method is suitable for testing images with complicated patterns.

Therefore, the proposed CIC holds superiority over the classical SIC in reconstruction performance and is especially appropriate for testing images with sharp edges, dark backgrounds, high contrast, grid shapes, and complicated patterns.

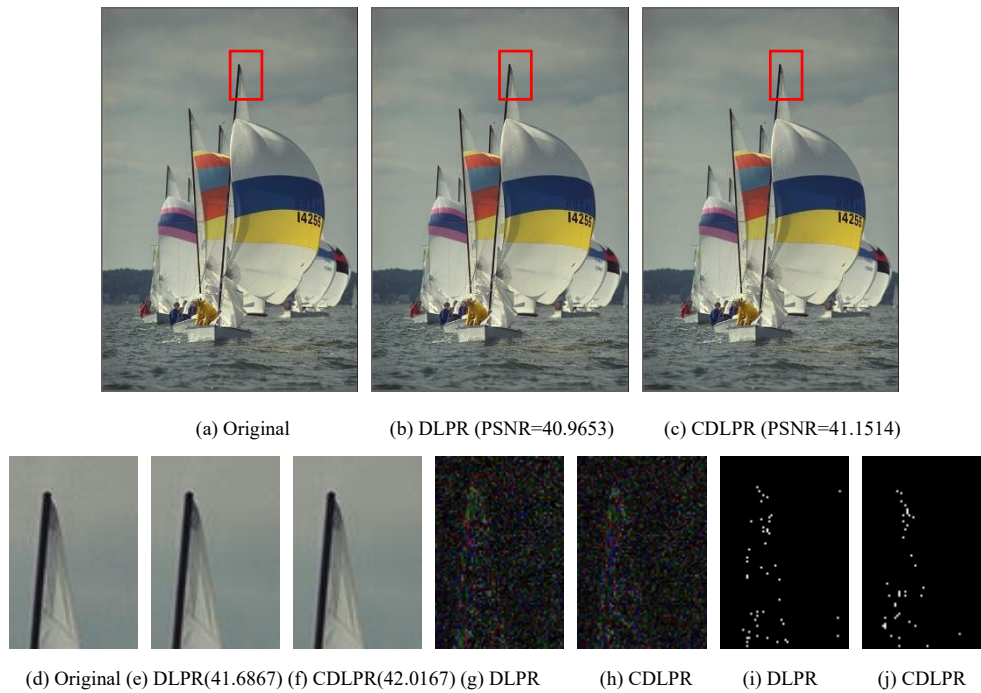


**Figure 9. Experimental results of DLPR and CDLPR with maximum PSNR increment on Kodak image dataset.**



**Figure 10. Experimental results of DLPR and CDLPR with maximum PSNR increment on CLIC2021 test image dataset.**

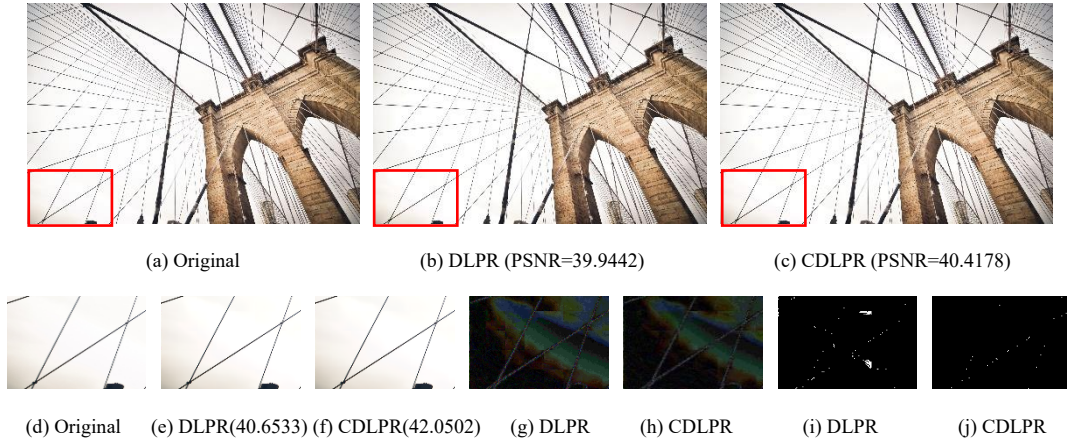


**Figure 11. Experimental results of DLPR and CDLPR with maximum PSNR increment on CLIC2021 validation image dataset.**

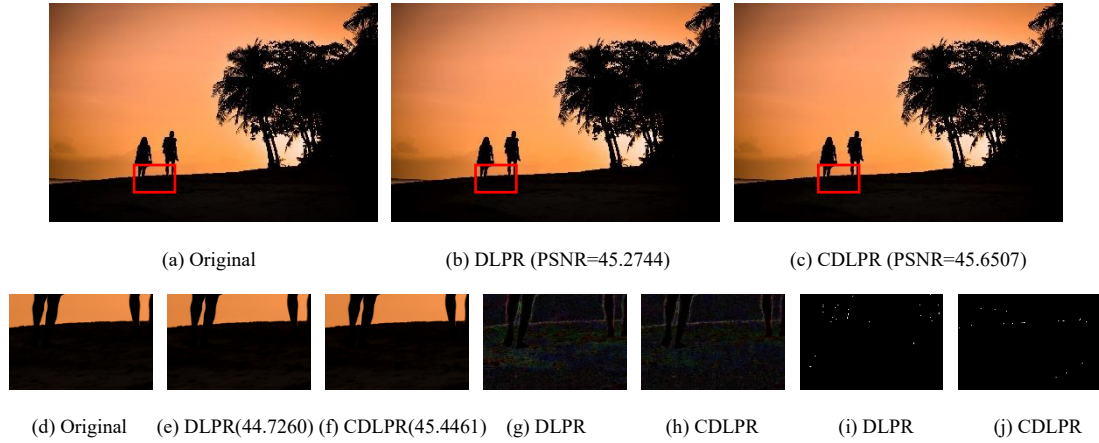


**Figure 12. Experimental results of DLPR and CDLPR with maximum PSNR increment on CLIC2022 validation image dataset.**

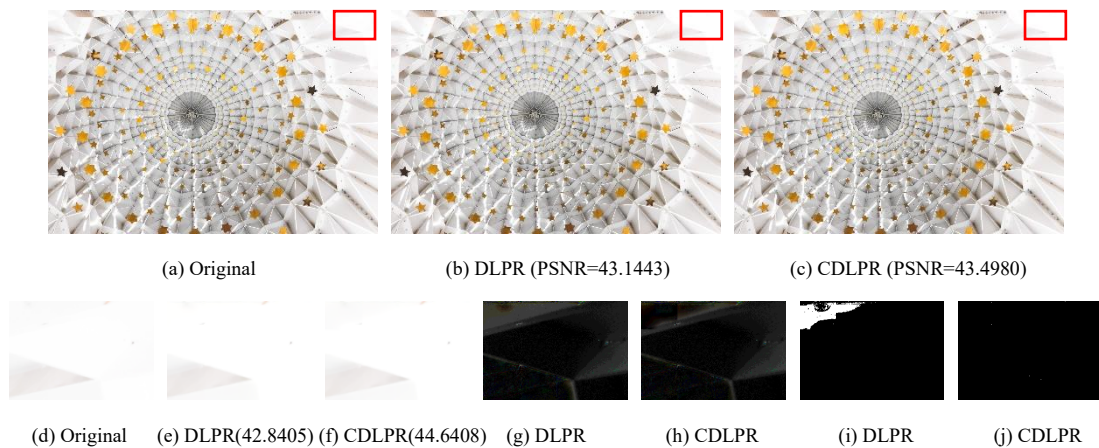


**Figure 13. Experimental results of DLPR and CDLPR with maximum PSNR increment on CLIC2024 validation image dataset.**

### 4.2.3 Experiment Results of Out-of-Sample

This experiment is arranged to assess the reconstruction performance for out-of-sample testing



images. Five typical out-of-sample testing images are selected in Figures 14 to 18. DLPR and CDLPR algorithms with quantization parameter  $\tau=7$  are chosen for performance comparison. The experimental results are listed in Table 9 and shown in Figures 14 to 18.

Table 10 shows that the proposed CDLPR achieves big gain of PSNR, small gain of SSIM, and almost the same BPSP, compared with the classical DLPR.  $\Delta_s$  is the maximum increment of PSNR or SSIM between CDLPR and DLPR for the subblocks of out-of-sample testing images.  $\Delta_s$  is also the maximum decrement of BPSP between CDLPR and DLPR for the subblocks of out-of-sample testing images.

**Table 10. Experimental results of DLPR and CDLPR for out-of-sample testing images.**

| Testing Images    |            | 1       | 2       | 3       | 4       | 5       |
|-------------------|------------|---------|---------|---------|---------|---------|
| PSNR $\uparrow$   | DLPR       | 43.8426 | 43.5019 | 38.7692 | 40.7594 | 42.1485 |
|                   | CDLPR      | 45.4137 | 44.9484 | 39.6996 | 41.7546 | 43.6161 |
|                   | $\Delta$   | 1.5711  | 1.4465  | 0.9304  | 0.9953  | 1.4676  |
|                   | $\Delta_s$ | 3.1953  | 1.9087  | 2.5383  | 2.4978  | 3.9212  |
| SSIM $\uparrow$   | DLPR       | 0.9675  | 0.9780  | 0.7085  | 0.8731  | 0.8925  |
|                   | CDLPR      | 0.9781  | 0.9881  | 0.7648  | 0.9088  | 0.9257  |
|                   | $\Delta$   | 0.0105  | 0.0101  | 0.0562  | 0.0357  | 0.0333  |
|                   | $\Delta_s$ | 0.0108  | 0.0211  | 0.0554  | 0.0314  | 0.2889  |
| BPSP $\downarrow$ | DLPR       | 0.2127  | 0.3318  | 0.1021  | 0.5056  | 0.2626  |
|                   | CDLPR      | 0.2127  | 0.3318  | 0.1021  | 0.4986  | 0.2626  |
|                   | $\Delta$   | 0.0000  | 0.0000  | 0.0000  | 0.0070  | 0.0000  |

Figure 14 shows the experimental results of out-of-sample testing image 1. Figure 14(a) is the original image, Figure 14(b) is the reconstruction image of DLPR, and Figure 14(c) is the reconstruction image of CDLPR. It is hard to discover the difference between Figure 14(b) and Figure 14(c). Figure 14(d) is the subblock of Figure 14(a), Figure 14(e) is the related subblock of Figure 14(b), and Figure 14(f) is the related subblock of Figure 14(c). Figure 14(d), (e), and (f) are marked with red boxes in Figure 14(a), (b), and (c) respectively. It is also hard to discover the difference between Figure 14(e) and Figure 14(f). Figure 14(g) is the absolute difference image block between Figure 14(e) and Figure 14(d), and Figure 14(h) is the absolute difference image block between Figure 14(f) and Figure 14(d). It is still hard to discover the difference between Figure 14(g) and Figure 14(h). Figure 14(i) is the logic difference image block between Figure 14(e) and Figure 14(d), and Figure 14(j) is the logic difference image block between Figure 14(f) and Figure 14(d). It is easy to discover the difference between Figure 14(i) and Figure 14(j). Figure 14(i) and Figure 14(j) indicate that the reconstruction image quality of CDLPR outperforms that of DLPR. Figure 14 indicates that the proposed method is effective for out-of-sample testing images with dark backgrounds and detailed foregrounds.

Figure 15 displays the experimental results of out-of-sample testing image 2. Figure 15(a) is the original image, Figure 15(b) is the restoration image of DLPR, and Figure 15(c) is the restoration image of CDLPR. It is difficult to seek out the discrepancy between Figure 15(b) and Figure 15(c). Figure 15(d) is the subblock of Figure 15(a), Figure 15(e) is the related subblock of Figure 15(b),



and Figure 15(f) is the related subblock of Figure 15(c). Figure 15(d), (e), and (f) are marked with red boxes in Figure 15(a), (b), and (c) respectively. It is also difficult to seek out the discrepancy between Figure 15(e) and Figure 15(f). Figure 15(g) is the absolute difference image block between Figure 15(e) and Figure 15(d), and Figure 15(h) is the absolute difference image block between Figure 15(f) and Figure 15(d). It is still difficult to seek out the discrepancy between Figure 15(g) and Figure 15(h). Figure 15(i) is the logic difference image block between Figure 15(e) and Figure 15(d), and Figure 15(j) is the logic difference image block between Figure 15(f) and Figure 15(d). It is effortless to seek out the discrepancy between Figure 15(i) and Figure 15(j). Figure 15(i) and Figure 15(j) reveal that the restoration image quality of CDLPR outbalances that of DLPR. Figure 15 shows that the proposed method is propitious to out-of-sample testing images with dark backgrounds and delicate foregrounds.

Figure 16 illustrates the experimental results of out-of-sample testing image 3. Figure 16(a) is the original image, Figure 16(b) is the recovery image of DLPR, and Figure 16(c) is the recovery image of CDLPR. It is tough to check the discrimination between Figure 16(b) and Figure 16(c). Figure 16(d) is the subblock of Figure 16(a), Figure 16(e) is the related subblock of Figure 16(b), and Figure 16(f) is the related subblock of Figure 16(c). Figure 16(d), (e), and (f) are marked with red boxes in Figure 16(a), (b), and (c) respectively. It is also tough to check the discrimination between Figure 16(e) and Figure 16(f). Figure 16(g) is the absolute difference image block between Figure 16(e) and Figure 16(d), and Figure 16(h) is the absolute difference image block between Figure 16(f) and Figure 16(d). It is still tough to check the discrimination between Figure 16(g) and Figure 16(h). Figure 16(i) is the logic difference image block between Figure 16(e) and Figure 16(d), and Figure 16(j) is the logic difference image block between Figure 16(f) and Figure 16(d). It is toil-less to check the discrimination between Figure 16(i) and Figure 16(j). Figure 16(i) and Figure 16(j) uncover that the recovery image quality of CDLPR overmatches that of DLPR. Figure 16 demonstrates that the proposed method is appropriate for out-of-sample testing images with dark backgrounds and exquisite foregrounds.

Figure 17 demonstrates the experimental results of out-of-sample testing image 4. Figure 17(a) is the original image, Figure 17(b) is the reestablishment image of DLPR, and Figure 17(c) is the reestablishment image of CDLPR. It is arduous to examine the distinction between Figure 17(b) and Figure 17(c). Figure 17(d) is the subblock of Figure 17(a), Figure 17(e) is the related subblock of Figure 17(b), and Figure 17(f) is the related subblock of Figure 17(c). Figure 17(d), (e), and (f) are marked with red boxes in Figure 17(a), (b), and (c) respectively. It is also arduous to examine the distinction between Figure 17(e) and Figure 17(f). Figure 17(g) is the absolute difference image block between Figure 17(e) and Figure 17(d), and Figure 17(h) is the absolute difference image block between Figure 17(f) and Figure 17(d). It is still arduous to examine the distinction between Figure 17(g) and Figure 17(h). Figure 17(i) is the logic difference image block between Figure 17(e) and Figure 17(d), and Figure 17(j) is the logic difference image block between Figure 17(f) and Figure 17(d). It is convenient to examine the distinction between Figure 17(i) and Figure 17(j). Figure 17(i) and Figure 17(j) disclose that the reestablishment image quality of CDLPR exceeds that of DLPR. Figure 17 indicates that the proposed method is fit for out-of-sample testing images with dark backgrounds and intricate patterns.

Figure 18 exhibits the experimental results of out-of-sample testing image 5. Figure 18(a) is the original image, Figure 18(b) is the rebuilding image of DLPR, and Figure 18(c) is the rebuilding image of CDLPR. It is formidable to inspect the distinguishing between Figure 18(b) and Figure 18(c). Figure 18(d) is the subblock of Figure 18(a), Figure 18(e) is the related subblock of Figure 18(b), and Figure 18(f) is the related subblock of Figure 18(c). Figure 18(d), (e), and (f) are marked with red boxes in Figure 18(a), (b), and (c) respectively. It is also formidable to inspect the distinguishing between Figure 18(e) and Figure 18(f). Figure 18(g) is the absolute difference image block between Figure 18(e) and Figure 18(d), and Figure 18(h) is the absolute difference image block between Figure 18(f) and Figure 18(d). It is still formidable to inspect the distinguishing between Figure 18(g) and Figure 18(h). Figure 18(i) is the logic difference image block between Figure 18(e) and Figure 18(d), and Figure 18(j) is the logic difference image block between Figure 18(f) and Figure 18(d). It is facile to inspect the distinguishing between Figure 18(i) and Figure 18(j). Figure 18(i) and Figure 18(j) expose that the rebuilding image quality of CDLPR surpasses that of DLPR. Figure 18 shows the proposed method is suitable for out-of-sample testing images with high contrast and tangled patterns.

All in all, the proposed CIC is superior to the classical SIC in reconstruction performance and is especially suitable for out-of-sample testing images with dark backgrounds, detailed foregrounds, complicated patterns, and high contrast.



**Figure 14. Experimental results of DLPR and CDLPR for out-of-sample testing image 1.**

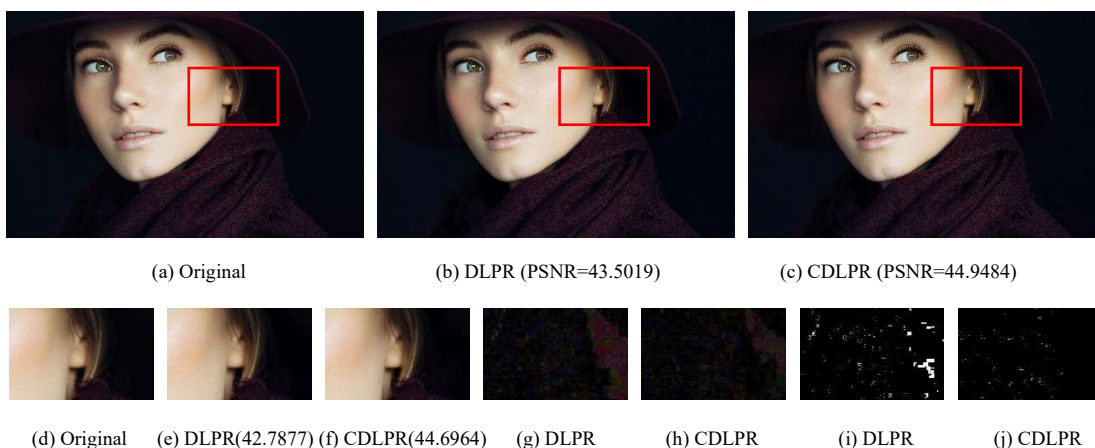


Figure 15. Experimental results of DLPR and CDLPR for out-of-sample testing image 2.

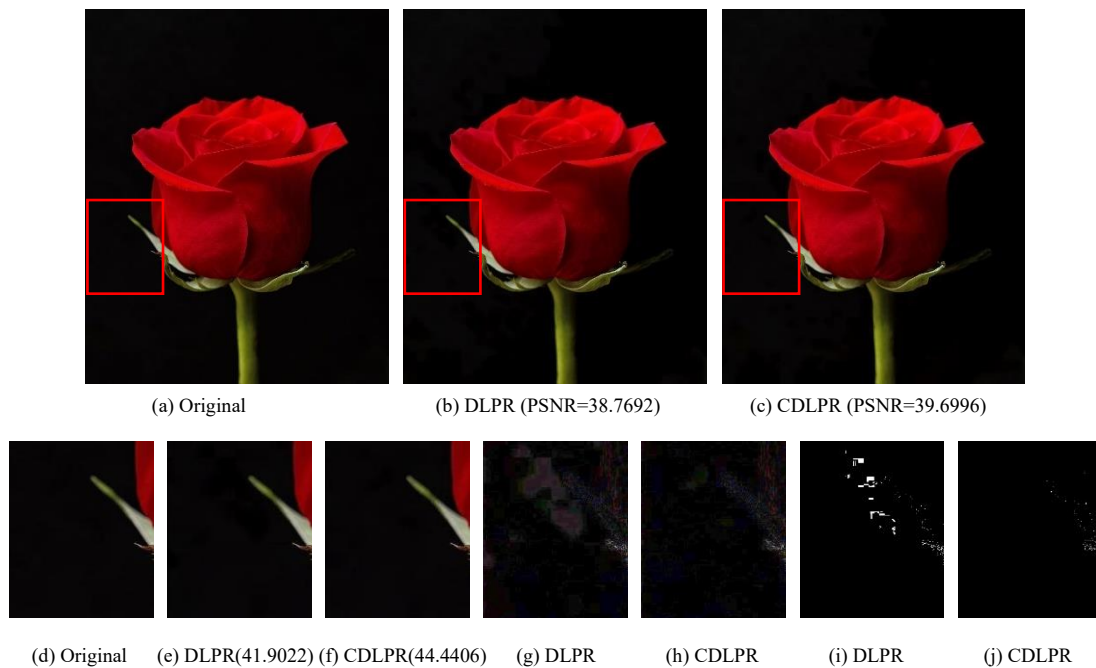


Figure 16. Experimental results of DLPR and CDLPR for out-of-sample testing image 3.

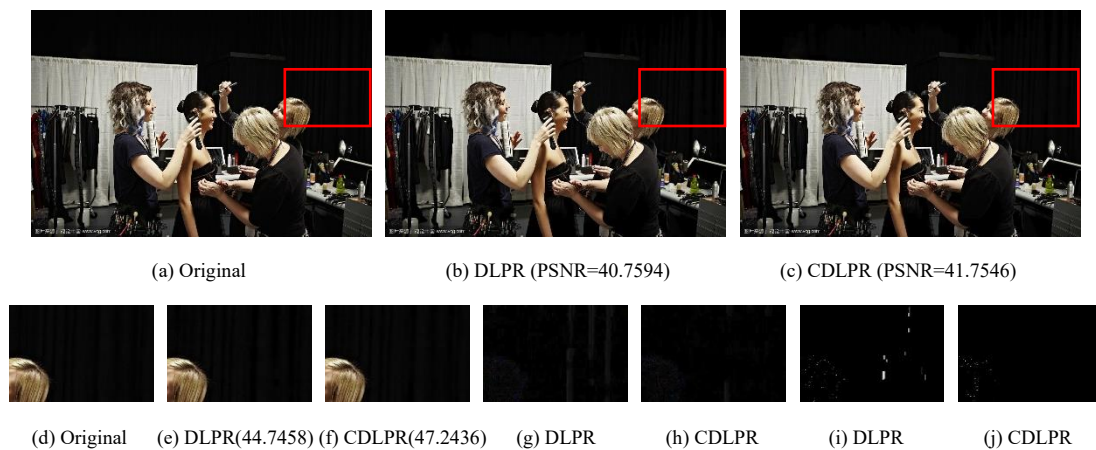
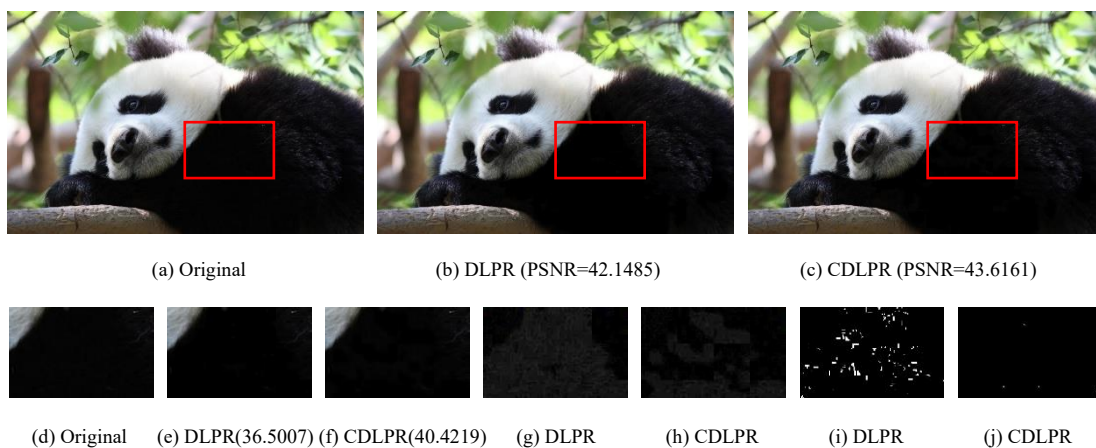


Figure 17. Experimental results of DLPR and CDLPR for out-of-sample testing image 4.



**Figure 18. Experimental results of DLPR and CDLPR for out-of-sample testing image 5.**

## **5 Conclusion**

This paper proposes the CIC framework which is a mixture of open-loop and closed-loop architectures. The open-loop structure comprises encoding and decoding units while the closed-loop structure comprises coding element, decoding element, summator, multiplier, and integrator. The CIC is described by a nonlinear loop equation which is resolved by linear approximation of Taylor series expansion, and the zero steady-state error of the CIC is mathematically proved. The proposed CIC can minimize the intrinsic difference between testing and training images and improve the performance of image reconstruction. The proposed CIC holds the property of plug-and-play and Post-Training and can be established on any existing advanced SIC algorithms. The experimental results on five public image compression datasets show that the proposed CIC outperforms five open-source state-of-the-art SIC approaches. Experimental results further show that the proposed CIC is particularly effective for out-of-sample testing images with dark backgrounds, sharp edges, high contrast, grid shapes, and complex patterns.

In our future work, the proposed CIC will be verified on more public image compression datasets and more existing open-source leading SIC methods. The proposed CIC will also be incorporated into In-Training procedure. Some advanced control theory, such as fuzzy logic, will further be considered in the proposed CIC.

## **Author Contributions**

Conceptualization, Honggui LI and Maria TROCAN; Methodology, Honggui LI, Beata MIKOVICOVA, and Dimitri GALAYKO; Writing, Honggui LI and Sinan CHEN; Experiment, Muhammad FAHIMULLAH and Nahid MD LOKMAN HOSSAIN; Supervision, Mohamad SAWAN. All authors have read and agreed to the published version of the manuscript.

## **Competing Interests**

The authors declare that they have no known competing financial interests or personal relationships that could have appeared to influence the work reported in this paper.

## **Acknowledgment**

The authors would very much like to thank all the authors of the competing algorithms for selflessly releasing their source codes of image super-resolution on the Microsoft GitHub website. The open-source codes allow us to easily implement the proposed algorithm depending on the competing algorithms. The authors also would very much like to express deep thanks to Google COLAB for its free GPU computing service.

## **References**

- [1] Noy S, Zhang W, Experimental Evidence on the Productivity Effects of Generative Artificial Intelligence, *SCIENCE*, 2023, 381(6654), 187-192.
- [2] Jamil S, Piran MJ, Rahman M, Kwon OJ, Learning-driven lossy image compression: A comprehensive survey, *ENGINEERING APPLICATIONS OF ARTIFICIAL INTELLIGENCE*, 2023,123(B), 106361.
- [3] Huang CH, Wu JL, Unveiling the Future of Human and Machine Coding: A Survey of End-to-End Learned Image Compression, *ENTROPY*, 2024, 26(5), 1-35.
- [4] Lungisani BA, Lebekwe CK, Zungeru AM, Yahya A, Image Compression Techniques in Wireless Sensor Networks: A Survey and Comparison, *IEEE ACCESS*, 2022, 10, 82511-82530.
- [5] Mishra D, Singh SK, Singh RK, Deep Architectures for Image Compression: A Critical Review, *SIGNAL PROCESSING*, 2022, 191, 108346, 1-15.
- [6] Li JY, Chen PG, Yu SZ, Liu S, Jia JY, MOODv2: Masked Image Modeling for Out-of-Distribution Detection, *IEEE TRANSACTIONS ON PATTERN ANALYSIS AND MACHINE INTELLIGENCE*, 2024, Early Access, 1-11.
- [7] Li SH, Dai WR, Fang YM, Zheng ZY, Fei W, Xiong HK, Zhang W, Revisiting Learned Image Compression with Statistical Measurement of Latent Representations, *IEEE TRANSACTIONS ON CIRCUITS AND SYSTEMS FOR VIDEO TECHNOLOGY*, 2024, 34(4), 2891-2907.
- [8] Tsubota K, Aizawa K, Content-Adaptive Optimization Framework for Universal Deep Image Compression, *IEICE TRANSACTIONS ON INFORMATION AND SYSTEMS*, 2024 E107(2), 201-211.
- [9] Zhu JM, Yang YQ, Zhang TP, Cao ZQ, Finite-Time Stability Control of Uncertain Nonlinear Systems With Self-Limiting Control Terms, *IEEE TRANSACTIONS ON NEURAL NETWORKS AND LEARNING SYSTEMS*, 2023, 34(11), 9514-9519.
- [10] Xia XN, Zhang TP, Kang GP, Fang Y, Adaptive Control of Uncertain Nonlinear Systems With Discontinuous Input and Time-Varying Input Delay, *IEEE TRANSACTIONS ON SYSTEMS MAN CYBERNETICS-SYSTEMS*, 2022, 52(11), 7248-7258.
- [11] Wei PX, Xie ZW, Li GB, Lin L, Taylor Neural Network for Real-World Image Super-Resolution, *IEEE TRANSACTIONS ON IMAGE PROCESSING*, 2023, 32, 1942-1951.
- [12] Bao YE, Tan W, Zheng LF, Meng FY, Liu W, Liang YS, Taylor Series Based Dual-Branch Transformation for Learned Image Compression, *SIGNAL PROCESSING*, 2023, 212, 109128, 1-15.
- [13] Ebner A, Haltmeier M, Plug-and-Play Image Reconstruction Is a Convergent Regularization Method, *IEEE TRANSACTIONS ON IMAGE PROCESSING*, 2024, 33, 1476-1486.
- [14] Chen Y, Gui XF, Zeng JS, Zhao XL, He W, Combining Low-Rank and Deep Plug-and-Play Priors for Snapshot Compressive Imaging, *IEEE TRANSACTIONS ON NEURAL NETWORKS AND LEARNING SYSTEMS*, 2023, Early Access, 1-14.
- [15] Wu TT, Wu WN, Yang Y, Fan FL, Zeng TY, Retinex Image Enhancement Based on Sequential Decomposition With a Plug-and-Play Framework, *IEEE TRANSACTIONS ON NEURAL NETWORKS AND LEARNING SYSTEMS*, 2023, Early Access, 1-14.
- [16] Kamilov US, Bouman CA, Buzzard GT, Wohlberg B, Plug-and-Play Methods for Integrating Physical and Learned Models in Computational Imaging: Theory, algorithms, and applications, *IEEE SIGNAL PROCESSING MAGAZINE*, 2023, 40(1), 85-97.
- [17] Zhang K, Li YW, Zuo WM, Zhang L, Van GL, Timofte R, Plug-and-Play Image Restoration with Deep Denoiser Prior, *IEEE TRANSACTIONS ON PATTERN ANALYSIS AND MACHINE*

INTELLIGENCE, 2022, 44(10), 6360-6376.

[18] Zandavi SM, Post-trained convolution networks for single image super-resolution, ARTIFICIAL INTELLIGENCE, 2023, 318, 103882, 1-15.

[19] Bai YC, Liu XM, Wang K, Ji XY, Wu XL, Gao W, Deep Lossy Plus Residual Coding for Lossless and Near-Lossless Image Compression, IEEE TRANSACTIONS ON PATTERN ANALYSIS AND MACHINE INTELLIGENCE, 2024, 46(5), 3577-3594.

[20] Yang RH, Mandt S, Lossy Image Compression with Conditional Diffusion Models, Advances in Neural Information Processing Systems, 2023, 36, 20241715986225, 37th Conference on Neural Information Processing Systems (NeurIPS 2023), December 10-16, 2023, New Orleans, LA, United States, arXiv e-print, arXiv:2209.06950, 2022, 1-25.

[21] Bai YC, Yang Xu, Liu XM, Jiang JJ, Wang YW, Ji XY, Gao W, Towards End-to-End Image Compression and Analysis with Transformers, Proceedings of the 36th AAAI Conference on Artificial Intelligence (AAAI 2022), 36, 104-112, February 22 - March 1, 2022, Virtual, Online, arXiv e-print, arXiv:2112.09300, 2021, 1-14.

[22] Zhang ZB, Esenlik S, Wu YJ, Wang M, Zhang K, Zhang L, End-to-End Learning-Based Image Compression With a Decoupled Framework, IEEE TRANSACTIONS ON CIRCUITS AND SYSTEMS FOR VIDEO TECHNOLOGY, 2024, 34(5), 3067-3081.

[23] Zhang DY, Li F, Liu M, Cong RM, Bai HH, Wang M, Zhao Y, Exploring Resolution Fields for Scalable Image Compression With Uncertainty Guidance, IEEE TRANSACTIONS ON CIRCUITS AND SYSTEMS FOR VIDEO TECHNOLOGY, 2024, 34(4), 2934-2948.

[24] Guerin ND Jr, da Silva RC, Macchiavello B, Learning-Based Image Compression With Parameter-Adaptive Rate-Constrained Loss, IEEE SIGNAL PROCESSING LETTERS, 2024, 31, 1099-1103.

[25] Zhang WC, Liu YJ, Chen LY, Shi JH, Hong XM, Wang XB, Semantically-Disentangled Progressive Image Compression for Deep Space Communications: Exploring the Ultra-Low Rate Regime, IEEE JOURNAL ON SELECTED AREAS IN COMMUNICATIONS, 2024, 42(5), 1130-1144.

[26] Fu HS, Liang F, Lin JP, Li B, Akbari M, Liang J, Zhang GH, Liu D, Tu CJ, Han JN, Learned Image Compression With Gaussian-Laplacian-Logistic Mixture Model and Concatenated Residual Modules, IEEE TRANSACTIONS ON IMAGE PROCESSING, 2023, 32, 2063-2076.

[27] Duan ZH, Lu M, Ma Z, Zhu FQ, Lossy Image Compression with Quantized Hierarchical VAEs, Proceedings of 2023 IEEE Winter Conference on Applications of Computer Vision (WACV 2023), 198-207, January 3-7, 2023, Waikoloa, HI, United states, arXiv e-print, arXiv:2208.13056, 2022, 1-15.

[28] Timur A, Vector Quantized Variational Image Compression, Research Report of Bayesian Methods of Machine Learning, Skolkovo Institute of Science and Technology, Moscow, Russia, 2022, 1-6.

[29] Cai SL, Chen LQ, Zhang ZJ, Zhao XY, Zhou JH, Peng YX, Yan LX, Zhong S, Zou X, I2C: Invertible Continuous Codec for High-Fidelity Variable-Rate Image Compression, IEEE TRANSACTIONS ON PATTERN ANALYSIS AND MACHINE INTELLIGENCE, 2024, 46 (6), 4262-4279.

[30] Fu HS, Liang F, Liang J, Li BL, Zhang GH, Han JN, Asymmetric Learned Image Compression With Multi-Scale Residual Block, Importance Scaling, and Post-Quantization Filtering, IEEE TRANSACTIONS ON CIRCUITS AND SYSTEMS FOR VIDEO TECHNOLOGY, 2023, 33(8),

4309-4321.

[31] Zhang G, Zhang XF, Tang L, Enhanced Quantified Local Implicit Neural Representation for Image Compression, IEEE SIGNAL PROCESSING LETTERS, 2023, 30, 1742-1746.

[32] Guo JY, Xu D, Lu G, CBANet: Toward Complexity and Bitrate Adaptive Deep Image Compression Using a Single Network, IEEE TRANSACTIONS ON IMAGE PROCESSING, 2023, 32, 2049-2062.

[33] Jiang ZY, Liu XH, Li AN, Wang GY, Enhancing High-Resolution Image Compression Through Local-Global Joint Attention Mechanism, IEEE SIGNAL PROCESSING LETTERS, 2024, 31, 1044-1048.

[34] Li B, Li YJ, Luo JC, Zhang XR, Li CY, Chenjin ZM, Liang Y, Learned Image Compression via Neighborhood-based Attention Optimization and Context Modeling with Multi-scale Guiding, ENGINEERING APPLICATIONS OF ARTIFICIAL INTELLIGENCE, 2024, 129, 107596, 1-15.

[35] Tang ZS, Wang HL, Yi XK, Zhang Y, Kwong S, Kuo CCJ, Joint Graph Attention and Asymmetric Convolutional Neural Network for Deep Image Compression, IEEE TRANSACTIONS ON CIRCUITS AND SYSTEMS FOR VIDEO TECHNOLOGY, 2023, 33(1), 421-433.

[36] Shi JQ, Lu M, Ma Z, Rate-Distortion Optimized Post-Training Quantization for Learned Image Compression, IEEE TRANSACTIONS ON CIRCUITS AND SYSTEMS FOR VIDEO TECHNOLOGY, 2024, 34 (5), 3082-3095.

[37] Duan ZH, Lu M, Ma J, Huang YN, Ma Z, Zhu FQ, QARV: Quantization-Aware ResNet VAE for Lossy Image Compression, IEEE TRANSACTIONS ON PATTERN ANALYSIS AND MACHINE INTELLIGENCE, 2024, 46(1), 436-450.

[38] Li SH, Li H, Dai WR, Li CL, Zou JN, Xiong HK, Learned Progressive Image Compression With Dead-Zone Quantizers, IEEE TRANSACTIONS ON CIRCUITS AND SYSTEMS FOR VIDEO TECHNOLOGY, 2023, 33(6), 2962-2978.

[39] Son H, Kim T, Lee H, Lee S, Enhanced Standard Compatible Image Compression Framework Based on Auxiliary Codec Networks, IEEE TRANSACTIONS ON IMAGE PROCESSING, 2022, 31, 664-677.

[40] Li JF, Liu XY, Gao YQ, Zhuo L, Zhang J, BARRN: A Blind Image Compression Artifact Reduction Network for Industrial IoT Systems, IEEE TRANSACTIONS ON INDUSTRIAL INFORMATICS, 2023, 19(9), 9479-9490.

[41] Ma L, Zhao YF, Peng PX, Tian YH, Sensitivity Decouple Learning for Image Compression Artifacts Reduction, IEEE TRANSACTIONS ON IMAGE PROCESSING, 2024, 33, 3620-3633.

[42] Hu JH, Luo GX, Wang B, Wu WM, Yang JH, Guo JD, Residual Network for Image Compression Artifact Reduction, INTERNATIONAL JOURNAL OF PATTERN RECOGNITION AND ARTIFICIAL INTELLIGENCE, 2024, 38(02), 2454001, 1-15.

[43] Chen HG, He XH, Yang H, Qing LB, Teng QZ, A Feature-Enriched Deep Convolutional Neural Network for JPEG Image Compression Artifacts Reduction and Its Applications, IEEE TRANSACTIONS ON NEURAL NETWORKS AND LEARNING SYSTEMS, 2022, 33(1), 430-444.

## Biographies





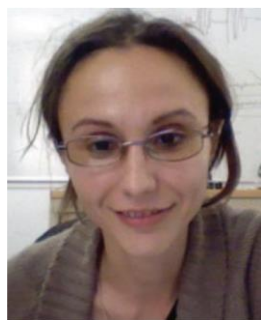
**Honggui LI** received a B.S. degree in electronic science and technology from Yangzhou University and received a Ph.D. degree in mechatronic engineering from Nanjing University of Science and Technology. He is a senior member of the Chinese Institute of Electronics. He is a visiting scholar and a post-doctoral fellow at Institut Supérieur d'Électronique de Paris for one year. He is an associate professor of electronic science and technology and a postgraduate supervisor of electronic science and technology at Yangzhou University. He is a reviewer for some international journals and conferences. He is the author of over 30 refereed journal and conference articles. His current research interests include machine learning, deep learning, computer vision, and embedded computing.



**Sinan CHEN** received a B.E. degree in electronics information engineering from Yangzhou University in China. He is now studying for a master's degree in integrated circuits engineering at Yangzhou University in China.



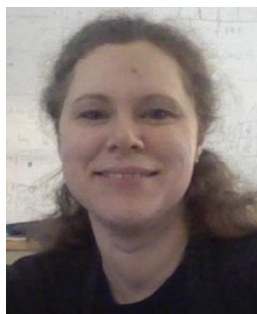
**Nahid MD LOKMAN HOSSAIN** received a B.S. degree in computer science and technology from Chongqing University of Posts and Telecommunications in China. He is now studying for a master's degree in software engineering at Yangzhou University in China. His research interests include machine learning, computer vision, innovation software, cloud computing, and big data.



**Maria TROCAN** received a M.Eng. in Electrical Engineering and Computer Science from the Politehnica University of Bucharest, a Ph.D. in Signal and Image Processing from Telecom ParisTech, and the Habilitation to Lead Researches (HDR) from Pierre & Marie Curie University (Paris 6). She has joined Joost - Netherlands, where she worked as a research engineer involved in the design and development of video transcoding systems. She is firstly Associate Professor, then Professor at Institut Supérieur d'Électronique de Paris (ISEP). She is an Associate Editor for the Springer Journal on Signal, Image and Video Processing and a Guest Editor for several journals (Analog Integrated Circuits and Signal Processing, IEEE Communications Magazine, etc.). She is an active member of IEEE France and served as a counselor for the ISEP IEEE Student Branch, IEEE France Vice-President responsible for Student Activities, and IEEE Circuits and Systems Board of Governors member, as Young Professionals representative. Her current research interests focus on image and video analysis & compression, sparse signal representations, machine



learning, and fuzzy inference.



**Beata MIKOVICOVA** received her B.Eng. and Ph.D. degrees in Electrical Engineering from Slovak Technical University in Bratislava. She joined Institut Supérieur d'Electronique de Paris (ISEP) as an Assistant Professor at the Telecommunications Department. She is a member of Signal, Image, and Telecommunications Department at ISEP. She is the International Mobility Manager at ISEP. Her research interests are in image processing, information theory, and digital communications. She has been involved in research projects related to signal processing for digital communications, detection, estimation, and biometrics.



**Muhammad FAHIMULLAH** received his B.S. degree in computer science from the University of Peshawar in Pakistan, his M.S. degree in software engineering from COMSATS University Islamabad in Pakistan, his M.S. degree in Software Engineering from Institut Supérieur d'Electronique de Paris (ISEP) in France. He is now studying for a Ph.D. degree in Software Engineering at ISEP. He joins ISEP as Dr. responsible for Cloud Computing-related activities.



**Dimitri GALAYKO** received a bachelor's degree from Odessa State Polytechnic University in Ukraine, a master's degree from the Institute of Applied Sciences of Lyon in France, and a Ph.D. degree from University of Lille in France. He made his Ph.D. thesis at the Institute of Microelectronics and Nanotechnologies. His Ph.D. dissertation was on the design of micro-electromechanical silicon filters and resonators for radio communications. He is a Professor at the LIP6 research laboratory of Sorbonne University in France. His research interests include the study, modeling, and design of nonlinear integrated circuits for sensor interfaces and mixed-signal applications. His research interests also include machine learning and fuzzy computing.



**Mohamad SAWAN** (Fellow, IEEE) received a Ph.D. degree in electrical engineering from the University of Sherbrooke, Sherbrooke, QC, Canada, in 1990. He was a Chair Professor awarded with the Canada Research Chair in Smart Medical Devices (2001–2015) and was leading the Microsystems Strategic Alliance of Quebec - ReSMiQ (1999–2018). He is a Professor of Microelectronics and Biomedical Engineering, in leave of absence from Polytechnique Montréal, Canada. He joined Westlake University, Hangzhou, China, in January 2019, where he is a Chair Professor, Founder, and Director of the Center for Biomedical Research And Innovation (CenBRAIN). He has published more than 800 peer-reviewed articles, two books, ten book chapters, and 12 patents. He founded and chaired the IEEE-Solid State Circuits Society Montreal Chapter (1999–2018) and founded the Polystim Neurotech Laboratory, Polytechnique Montréal (1994–

present), including two major research infrastructures intended to build advanced Medical devices. He is the Founder of the International IEEE-NEWCAS Conference, and the Co-Founder of the International IEEE-BioCAS, ICECS, and LSC conferences. He is a Fellow of the Royal Society of Canada, a Fellow of the Canadian Academy of Engineering, and a Fellow of the Engineering Institutes of Canada. He is also the “Officer” of the National Order of Quebec. He has served as a member of the Board of Governors (2014–2018). He is the Vice-President of Publications (2019–present) of the IEEE CAS Society. He received several awards, among them the Queen Elizabeth II Golden Jubilee Medal, the Barbara Turnbull 2003 Award for spinal cord research, the Bombardier and Jacques-Rousseau Awards for academic achievements, the Shanghai International Collaboration Award, and the Medal of Merit from the President of Lebanon for his outstanding contributions. He was the Deputy Editor-in-Chief of the IEEE TRANSACTIONS ON CIRCUITS AND SYSTEMS-II: EXPRESS BRIEFS (2010–2013); the Co-Founder, an Associate Editor, and the Editor-in-Chief of the IEEE TRANSACTIONS ON BIOMEDICAL CIRCUITS AND SYSTEMS; an Associate Editor of the IEEE TRANSACTIONS ON BIOMEDICALS ENGINEERING; and the International Journal of Circuit Theory and Applications.